Large eddy simulations of EUCLIPSE/GASS Lagrangian stratocumulus to cumulus transitions: Mean state, turbulence, and decoupling.

Stephan R. de Roode*, Irina Sandu[†], Johan J. van der Dussen[‡], Andrew S. Ackerman[§], Peter Blossey[¶], Dorota Jarecka[‖], Adrian Lock[**], A. Pier Siebesma[††] and Bjorn Stevens[‡‡]

Manuscript accepted for publication in the J. Atmos. Sci., 9 March 2016

*Corresponding author address: Stephan R. de Roode, s.r.deroode@tudelft.nl, Department of Geoscience and Remote Sensing, Delft University of Technology, Delft, The Netherlands.

[†] *MPI for Meteorology, Hamburg, Germany, and ECMWF, Reading, United Kingdom*

[‡] *Delft University of Technology, Delft, The Netherlands*

[§] *NASA Goddard Institute for Space Studies, New York, USA*

[¶] *Univ. of Washington, Seattle (WA), USA*

[‖] *Univ. of Warsaw, Warsaw, Poland*

[**] *UKMO, Exeter, United Kingdom*

[††] *Delft University of Technology, Delft, The Netherlands, and KNMI, De Bilt, The Netherlands*

[‡‡] *MPI for Meteorology, Hamburg, Germany*

ABSTRACT

Results of four Lagrangian stratocumulus to shallow cumulus transition cases as obtained from six different large-eddy simulation models are presented. The model output is remarkably consistent in terms of the representation of the evolution of the mean state, which is characterized by a stratocumulus cloud layer that raises with time and which warms and dries relative to the subcloud layer. Also the effect of the diurnal insolation on cloud-top entrainment and the moisture flux at the top of the subcloud layer are consistently captured by the models. For some cases the models diverge in terms of the liquid water path (LWP) during nighttime which can be explained from the difference in the sign of the buoyancy flux at cloud base. If the subcloud buoyancy fluxes are positive, turbulence sustains a vertically well mixed layer causing a cloud layer that is relatively cold and moist and consequently having a high LWP. After some simulation time all cases exhibit subcloud layer dynamics which appear to be similar to those of the dry convective boundary layer. The humidity flux from the subcloud towards the stratocumulus cloud layer, which is one the major sources of stratocumulus cloud liquid water, is larger during the night than during the day. The sensible heat flux becomes constant in time whereas the latent heat flux tends to increase during the transition. These findings are explained from a budget analysis of the subcloud layer.

1. Introduction

Stratocumulus cloud layers are frequently found over relatively cold parts of the subtropical oceans and in the presence of large-scale subsidence. These conditions favor the formation of a thermal inversion, which acts to trap moisture giving rise to extended fields of stratocumulus (Wood 2012). Although the depth of stratocumulus layers is relatively shallow, typically of the order of a few hundreds of meters, they strongly reflect downwelling solar radiation. During the equatorwards transport by the prevailing trade winds over increasing sea surface temperatures the subtropical stratocumulus cloud fields gradually break up and are replaced by shallow cumulus clouds. If a model is not able to capture this stratocumulus to cumulus cloud transition (SCT) this will lead to significant errors in the radiative fluxes received at the ground surface. This is a critical problem as climate models disagree on the change of the subtropical low cloud amount under a global warming scenario, which gives rise to a considerable amount of uncertainty in projections of the future global mean temperature (Bony and Dufresne 2005; Webb et al. 2013; Tsushima et al. 2015).

To investigate the change of the low cloud amount under an idealized warming scenario Zhang et al. (2013) performed experiments with single-column model (SCM) versions of climate models and large-eddy simulation (LES) models. The LES results point to a reduction of the amount of subtropical marine low clouds in a warmer climate (Blossey et al. 2013; Van der Dussen et al. 2015; Bretherton 2015). The study by Zhang et al. (2013), and follow-up studies by Dal Gesso et al. (2014) and Dal Gesso et al. (2015) report a wide scatter in the change of the steady-state subtropical low cloud amount in the SCM results. These results actually give rise to the question how large-scale forcing conditions like the sea surface temperature, free tropospheric temperature and humidity and the large-scale subsidence determine control the SCT.

The SCT has been the subject of several observational (e.g. Albrecht et al. (1995), Bretherton et al. (1995), De Roode and Duynkerke (1997), Sandu et al. (2010)) and modelling studies (e.g. Krueger et al. (1995), Sandu and Stevens (2011) and Van der Dussen et al. (2013)). Chung et al. (2012) studied a series of steady-state LESs in the SCT regime which can be interpreted as an Eulerian view of the transition. These studies helped to develop a conceptual view of this transition. According to this model the cloud breakup is fundamentally driven by the increasing SST. Convective activity driven by surface evaporation increases as the air advects over warmer waters. The strengthening of convectively driven turbulence enhances the entrainment of warm and dry free-tropospheric air at cloud top, which leads to a higher virtual potential temperature of the stratocumulus cloud layer as compared to the subcloud layer. This stratification prevents surface driven thermals to reach the stratocumulus cloud, except if they become saturated. In that case latent heat release due to condensation of water allows the plumes to rise as positively buoyant cumulus clouds, which may penetrate the stratocumulus cloud layer to inject it with moisture from below (Wang and Lenschow 1995; Miller and Albrecht 1995; De Roode and Duynkerke 1996; Van der Dussen et al. 2014). Meanwhile, the stratocumulus gradually thins if entrainment of relatively warm and dry free tropospheric air dominates the longwave radiative cooling at cloud top and the moisture supply from below. The stratocumulus finally dissipates into thin and broken patches, penetrated from below by cumulus clouds.

To assess whether LES models are capable of faithfully capturing the dynamics of low clouds, several modeling intercomparison studies have been performed, some of which focussed on stratocumulus (Moeng et al. 1996; Duynkerke et al. 1999, 2004; Stevens et al. 2005a; Ackerman et al. 2009), while other studies were dedicated to shallow cumulus (Siebesma et al. 2003; VanZanten et al. 2011), or cumulus penetrating stratocumulus (Stevens et al. 2001). More recently, four Lagrangian stratocumulus to cumulus transition cases were proposed to evaluate how well models do in terms of the transition between the two regimes. This intercomparison study was performed in the framework of the Global Energy and Water Cycle Exchanges Project (GEWEX) Global Atmospheric System Studies (GASS) and the European Union Cloud Intercomparison, Process Study & Evaluation Project (EUCLIPSE).

Three of the transition cases were based on the "Composite" view of this transition build using state of the art reanalysis and satelite data (Sandu et al. 2010), while a fourth one revisited the SCM intercomparison case based on the ASTEX campaign (Bretherton et al. 1999). While ASTEX offers the opportunity to evaluate models against in situ data, the set of "Composite" transitions represents a more idealized framework for model evaluation, which offers the possibility of comparing the models for a variety of SCT cases, which differ for example in terms of amplitude or timescale of the transition.

This paper discusses the representation of the four Lagrangian SCT cases in six different LES models. The Lagrangian approach means that an air mass is followed as it is being advected by the mean wind from the subtropics towards the equator over an increasingly warmer SST. Superposed to this change in the surface forcing the air mass is being heated by absorption of solar radiation during daytime. The paper is organized as follows. In Section 2 the cases and the LES models are introduced. Section 3 discusses the LES results with an emphasis on the development of the two-layer structure of the boundary layer. This decoupled structure motivates to analyse the thermodynamic budgets of the two layers separately. The contribution of various processes such as entrainment, turbulent fluxes at the cloud base and radiation to the stratocumulus cloud layer evolution is presented in Section 4. Section 5 analyses the heat and moisture budgets of the subcloud layer and explains the time evolution of the surface fluxes of heat and moisture. Section 6 discusses and summarizes the main findings.

2. Set-up of the experiments

In this intercomparison case a so-called Lagrangian approach is applied which means that an air mass is followed as it is being advected by the mean wind allowing to study the SCT in a single simulation (Schubert et al. 1979). The horizontal advection term in the conservation equations for heat and moisture may be assumed to be zero in the simulations as the air parcel is followed along its trajectory. This assumption is acceptable as long as the vertical wind shear is negligibly small.

a. Summary of the Lagrangian stratocumulus transition cases

Three "Composite" cases representing SCTs of varying speed were built based on the observational study of Sandu et al. (2010). In that study, a large number of Lagrangian trajectories of air parcels in four subtropical oceans were computed using the wind fields provided by reanalysis of past observations and the evolution of the cloud and of its environment along each of these individual trajectories was documented from satellite data sets and meteorological reanalysis (Moderate Resolution Imaging Spectroradiometer (MODIS), Level 3 data for cloud properties, and European Centre for Medium-Range Weather Forecasts (ECMWF) Interim Re-Analysis (ERA-Interim, Simmons et al. (2007)) for environmental properties). This study suggested that averaged forcings can be considered as representative of individual trajectories, and can therefore be used to initialize numerical simulations of the transition between the two cloud regimes. Building on these findings, a Composite of the large-scale conditions encountered along the trajectories for the North East Pacific (NEP) during June-July-August 2006 and 2007 were used to set up a case study of the SCT, that will be referred to hereafter as the reference case study and is further described in Sandu and Stevens (2011). Two variations of this reference case corresponding to a faster, and respectively, to a slower transition in cloud fraction were also derived for the intercomparison study (and are also described in Sandu and Stevens (2011)). For that, the transitions analyzed for the NEP during June-July-August 2006 and 2007 were divided into three categories (fast, intermediate and slow), on the basis of the mean cloud fraction over the first 48 hours. The initial profiles and the large-scale conditions for each of the three cases represent the medians of the distributions of the various properties obtained for respective subset of trajectories.

The set-up of the fourth SCT case is described in detail by Van der Dussen et al. (2013). This case is based on observations collected during the first ASTEX Lagrangian experiment (Albrecht et al. 1995; Bretherton et al. 1995; De Roode and Duynkerke 1997) and large-scale forcing conditions as obtained from ERA-Interim. Since the set-up of the Composite cases is somewhat idealized, and because the ASTEX case particularly differs from the Composite cases in terms of precipitation and its relatively cold and moist free troposphere, we think is useful to discuss its results along with the results from the Composite cases.

The initial vertical profiles of the liquid water potential temperature (θ_l), total water specific humidity (q_t) and the horizontal wind velocity components (U and V, respectively) for the four different SCT cases are shown in Fig. 1. The ASTEX case has the smallest value for the initial inversion jump in the liquid water potential temperature, which gradually increases in magnitude for the Fast, Reference and Slow cases, respectively. The inversion jumps in the total specific humidities are also different for each case, with the Slow case having the driest free atmosphere. The input files provided on the EUCLIPSE website[1] include vertical profiles of quantities like temperature, humidity and ozone up to the stratosphere, which is necessary for radiative transfer computations. The transfer of solar radiation is calculated on the basis of a fixed latitude and longitude. Because the models applied their own radiative transfer code, the radiative fluxes entering the top of the LES domain differed among the models, despite that they all used the same prescribed vertical profiles for the atmospheric column above. The prescribed SST increases with time for each case, which reflects the Lagrangian equatorwards advection of the simulated air mass (see Fig. 2). The LES models compute the sensible and latent heat fluxes (SHF and LHF, respectively) from the prescribed time-dependent SST, a fixed value for the surface roughness length, $z_0 = 2 \times 10^{-4}$ m, but each with its own implementation of the Monin-Obukhov similarity theory.

For the ASTEX case the large-scale divergence gradually decreases with time, and the observed weakening of the wind velocities is taken into account by a time-varying geostrophic forcing (Van der Dussen et al. 2013). For the Composite cases the large-scale divergence and the geostrophic forcing are constant in time, where the geostrophic winds are the same as the initial profiles of the horizontal wind velocity components shown in Fig. 1. Although

[1] http://www.euclipse.nl

the trajectories for the Composite cases are simulated during the same period of time they have slightly different lengths as their horizontal wind speeds are not the same. The four Lagrangians also assume a constant surface pressure (see Table 1). The ASTEX and the three Composite cases last 40 hours and three days, respectively, as these are the timescales during which the bulk of the transition in cloud cover takes place.

b. Participating large-eddy simulation models and data output

Table 2 lists the models and their acronyms, along with contributors from each participating group, as well as the main references to the models. The vertical grid resolution in the lower 540 m is $\Delta z = 15$ m. To represent the sharp inversion layer capping the cloud layer the vertical resolution is gradually refined only above this height, and between 645 and 2400 m $\Delta z = 5$ m. The horizontal domain size is 4.48×4.48 km^2 and the number of grid points in the horizontal directions is $N_x = N_y = 128$, implying a horizontal grid spacing $\Delta x = \Delta y = 35$ m.

For each case six large-eddy simulations, each performed with a different code, are presented. Every code includes a detailed parameterization scheme for radiation and ice-free cloud microphysical processes, where the latter uses a fixed value for the cloud droplet concentration number $N_\mathrm{d} = 100$ cm^{-3}.

Because the lower tropospheric stability, defined as the difference between the potential temperature at the 700 hPa pressure level and the ground surface (Klein and Hartmann 1993), is key for the evolution of the SCT, a realistic tendency of the free tropospheric temperature is needed, in particular as the simulations were performed for a period of two or three days. Therefore, in contrast to many past studies, all models applied a full radiation code.

To compare the modeling results time series of scalars and hourly-mean vertical profiles according to the data protocol proposed by VanZanten et al. (2011) were provided by the modellers. Here it is important to note that liquid water (q_l) is defined to include cloud (q_c)

and rain water (q_r), $q_l = q_c + q_r$, with rain water being defined as drops having a diameter of 80 μm or larger. In the computation of the cloud fraction and cloud cover a grid cell is defined to be cloudy if $q_c > 10^{-5}$ kg/kg. Irrespective of whether a model includes rainwater in its internal representation of the liquid water potential temperature and the total specific humidity, rain water is included in the profiles of these variables and their fluxes.

3. Evolution of the mean state and turbulence structure

a. Time series

We start our analysis by inspection of the time evolution of the boundary layer, cloud amount, and the surface fluxes of sensible and latent heat (see Fig. 3). The time variable in the figure is set such that at the first occasion of local noon $t = 0$. Nighttime periods (denoted by 'N1', 'N2' and 'N3' at the top of Fig. 3h) are indicated by the grey vertical bands in the plots according to the simulation periods summarized in Table 3. For each LES model, and for each daytime and nighttime period we calculated time-mean results. To get an appreciation of the spread in the modelling results, Table 4 presents the overall LES mean values and standard deviations. Note that because during the first two hours of the simulations the turbulence has not fully developed yet, the results during this spin-up period were not used.

In brief, the results show that for all cases the cloud-topped boundary layer is gradually deepening with time, while the cumulus cloud base height reaches an approximate steady state. The effect of the diurnal variation of the solar radiation is clearly found from the time series of the LWP. Due to the absorption of solar radiation in the cloud layer the LWP has reduced values during daytime. The cloud layer breaks up during the second daytime period 'D2' for the Fast case, although it tends to recover to a closed cloud deck during the second night 'N2', except for MOLEM. The Slow case appears to maintain an almost closed cloud deck during the entire simulation period. For all SCTs the entrainment velocity is much larger during nighttime than during the day. Finally, for the Composite cases the surface evaporation gradually increases whereas the sensible heat flux remains rather small.

A closer inspection reveals that during local noon the growth of the inversion height becomes very small for the Composite cases, which is due to a reduced cloud-top entrainment rate whereas the subsidence keeps pushing down the boundary-layer top (see Figs. 3a-d). The variation in the boundary layer depth as represented by the standard deviation $\sigma_{\mathrm{z_i}}$ computed from the six model results also gradually increases with time (see Table 4). Given the myriad of physical processes that control the boundary layer depth (e.g. turbulence, radiation, entrainment and drizzle), the values of $\sigma_{\mathrm{z_i}}$ can be considered as relatively small, with maximum values of 100 m except for the Fast case which gives a value of 200 m during the third nighttime period 'N3'. The height of the lowest cumulus cloud base ($z_{\mathrm{cu,base}}$) is very consistently represented among the models, its standard deviation being less than 50 m. We find an overall relatively small increase of $z_{\mathrm{cu,base}}$ during the first part of the simulations, and during the second part it becomes almost constant in time.

By contrast, the intermodel spread in the cloud liquid water path (LWP) is relatively large particularly during the night (see Figs. 3e-h) similar to what was found in the stratocumulus model intercomparison study by Stevens et al. (2005a). The LES agree fairly well in terms of the representation of the diurnal variation of the LWP, although the amplitude is larger in the MPI/UCLA, DHARMA and EULAG models. The latter model explains a significant part of σ_{LWP}, which is relatively large as compared to the mean value, in particular during nighttime.

MOLEM and EULAG have a consistently different longwave radiative forcing for the three Composite cases as compared to the other LES models which results are very similar. For example, during the first night of the Composite cases the longwave radiative flux divergence in the cloud layer is about 5 Wm^{-2} smaller in MOLEM and about 10 Wm^{-2} larger in EULAG. The effect of the differences in the longwave radiative cooling on the cloud layer evolution is discussed in detail in Section 5. Figs. 3i-l show the time evolution of the cloud cover. Only in the EULAG model a solid cloud is maintained for all SCTs which possibly results from the imposed stronger cloud longwave radiative cooling. In the other models the stratocumulus starts to break up some hours after sun rise due to the absorption of solar radiation in the cloud layer (Nicholls 1984). Most of the time the stratocumulus is able to recover to a closed-cell cloud deck after sunset. The difference between the three Composite cases becomes clear as the cloud cover tends to reduce more rapidly for the Fast case compared to the Reference or Slow cases, which is in a rough agreement with estimations of cloud cover from MODIS. However the inter-model differences in the daytime cloud cover are rather large. For example, for the Fast and Reference cases the standard deviation of the cloud cover has maximum values during the third daytime period 'D3'.

The absorption of the solar radiation leads to the warming and the thinning of the cloud layer. The absorption of solar radiation in the cloud layer counteracts the longwave radiative cooling at the cloud top. The stabilization of the cloud layer during daytime tends to weaken the buoyancy production of turbulence, which in turn causes a reduction in the entrainment velocity. If we compare the entrainment velocity for the four cases, we find smaller values for a stronger thermal stratification as measured by the inversion jump values of θ_l. During the first nighttime period 'N1' the entrainment rate is largest for the ASTEX case, and gradually becomes smaller for the Fast, Reference and Slow cases, respectively. There is a good agreement in the modelled entrainment velocity, with a maximum standard deviation of about 1 mm s^{-1} (see Figs. 3m-p and Table 4).

The LES models give SHF values that are less than 10 Wm^{-2} (see Figs. 3q-t). The LHF tends to increase with time (see Figs. 3u-x), except for the ASTEX case for which a flattening of the temporal SST increase and a weakening geostrophic forcing yields lower wind velocities and consequently lower LHF values. The Composite cases exhibit a gradual increasing trend in the LHF, with an imposed diurnal cycle in which the flux increases faster during the night than during the day. The standard deviation of the LHF is within 10 Wm^{-2}.

Although the bulk features of the time variation of the cloud structure and the differences between the four cases are consistently represented, the variation in the cloud cover and the LWP leads to a rather large value for the standard deviation of the net shortwave radiation at the surface, with a maximum value of 80 $\mathrm{Wm^{-2}}$ during the third daytime period 'D3' for the Fast case. During the entire simulation period the standard deviation of the net longwave radiation at the surface is within 10 $\mathrm{Wm^{-2}}$.

b. Boundary-layer decoupling

Hourly mean vertical profiles of θ_l and q_t obtained from the Fast case 48 hours from local noon are shown in Fig. 4. The stratocumulus layer has a higher θ_l and a lower q_t than the subcloud layer. The subcloud and cloud layer each are rather well mixed vertically. The lowest inversion height is found in MOLEM, and the stronger longwave radiative cloud layer cooling imposed in the EULAG model causes a much higher inversion layer height due to a larger entrainment rate (Figs. 3m-p). At this time, all models show a broken stratocumulus cloud deck, with the cloud fraction varying roughly between 0.05 and 0.78, except for EULAG which maintains an almost closed cloud deck for all the SCTs. The differences in the horizontal wind velocity components across the inversion are small. This is also the case for the Slow and Reference cases where the jumps are smaller than 2 $\mathrm{ms^{-1}}$.

The different evolutions in θ_l and q_t in subcloud and cloud layers are illustrated in Fig. 5. We use the subscript 'ml' to denote the subcloud mixed-layer mean value. It is computed from the mean between the first level above the surface and the cumulus cloud base height h. Likewise we use the subscript 'cld' to indicate the stratocumulus mean value between its mean base and top heights. As an easy reference the values at the surface and just above the inversion are also shown in the figure, and are indicated by subscripts 'sfc' and z_i^+, respectively. The mean values of θ_l in the subcloud and stratocumulus cloud layers both increase in time, with $\theta_\mathrm{l,ml}$ roughly following the trend of the surface value, and $\theta_\mathrm{l,cld}$ increasing at a slightly faster pace. In contrast to $q_\mathrm{t,ml}$, $q_\mathrm{t,cld}$ shows a drying trend, which implies that the drying of the stratocumulus cloud layer by entrainment and drizzle is stronger than the moisture input by the updrafts from the subcloud layer.

After some simulation time the vertical profiles of θ_l and q_t all resemble a decoupled boundary layer structure, with a cloud layer that is relatively warm and dry with respect to the subcloud layer (Nicholls 1984; Bretherton and Wyant 1997; Stevens 2000; Wood and Bretherton 2004). A convenient way to measure the degree of decoupling is given by Park et al. (2004) who defined the following decoupling parameter,

$$\alpha_\psi = \frac{\psi_\mathrm{cld} - \psi_\mathrm{ml}}{\psi(z_\mathrm{i}^+) - \psi_\mathrm{ml}}, \qquad (1)$$

with $\psi \in \{\theta_\mathrm{l}, q_\mathrm{t}\}$, and z_i^+ the height just above the inversion layer. The decoupling parameter is equal to zero if the boundary layer is well mixed, i.e. θ_l and q_t constant with height.

Fig. 6 compares the decoupling parameters α_{q_t} and $\alpha_{\theta_\mathrm{l}}$ as found from the LES results with a fit of α_{q_t} that was obtained from aircraft observations analyzed by Wood and Bretherton (2004), their Fig. 5. Both the observations and the LES results suggest a stronger decoupling for deeper boundary layers, as measured by larger values of α_{q_t} and $\alpha_{\theta_\mathrm{l}}$. The results presented in Table 2 of Wood and Bretherton (2004) appear to give a somewhat smaller difference between α_{q_t} and $\alpha_{\theta_\mathrm{l}}$ than the LES results.

Large values of the decoupling parameters indicate that the cloud layer is relatively warm and dry with respect to the subcloud layer. Because a high temperature or a low total water amount in the cloud tend to reduce the cloud liquid water content, we will now take a closer look at the time evolution of the decoupling parameters. In particular, we will inspect the results for the Slow case which shows a rather large scatter in the nighttime LWP values among the six LES. The gradual deepening of the boundary layer is reflected in the gradual increase of α_{q_t} and $\alpha_{\theta_\mathrm{l}}$ with time (see Fig. 7). However, during the first nighttime period the boundary layer gets back to a very well mixed vertical structure, while during the second nighttime period a strong variation in the degree in the decoupling is observed. For the latter period the DHARMA and MPI/UCLA models show an almost perfectly vertically mixed boundary layer, whereas the boundary layer remains rather strongly decoupled in DALES.

Inspection of the LWP values confirm its strong correlation with the degree of decoupling, with DHARMA and MPI/UCLA having the largest LWP values and the smallest values for the decoupling parameters.

c. *Turbulence*

The θ_l and q_t fields presented in Fig. 8 show a distinct three layer structure with a very sharp inversion layer that separates the stratocumulus layer from the dry free troposphere. The top of the subcloud layer itself is much more diffuse. The encircled numbers '1' and '2' are near rising subcloud plumes that become saturated and ascend further as cumulus clouds thereby transporting subcloud layer moisture towards the stratocumulus. Interestingly, area '3' is in an area above cumulus clouds, and shows sinking motions near two holes in the stratocumulus cloud deck, that resulted from evaporation of cloud water by entrainment of free tropospheric air (Gerber et al. 2005; De Roode and Wang 2007; de Lozar and Mellado 2015). Turbulence in clear air patches above the subcloud layer was also detected from aircraft observations during ASTEX (De Roode and Duynkerke 1996).

The findings presented so far suggest that the inter-model spread in the LWP during nighttime can be linked to the various strengths of the decoupling between the cloud and the subcloud layer. Stevens et al. (2005b) reported similar findings for the DYCOMS-II nighttime stratocumulus LES intercomparison case. They found a strong link between the buoyancy flux profile, the vertical velocity variance, and the degree of decoupling. It is therefore instructive to repeat their analysis by inspecting the turbulence profiles for the SCTs. Fig. 9 shows hourly-mean vertical profiles of the vertical velocity variance $\overline{w'w'}$, the virtual potential temperature flux $\overline{w'\theta_\mathrm{v}'}$, the vertical flux of total water specific humidity $\overline{w'q_\mathrm{t}'}$, and the turbulent kinetic energy (TKE) for the Slow case. Note that the fluxes of the virtual potential temperature and the buoyancy b are proportional, $\overline{w'b'} = \beta\overline{w'\theta_\mathrm{v}'}$, with $\beta = g/\theta_0$, g the acceleration due to gravity and θ_0 a constant reference temperature.

The surface buoyancy fluxes are positive. Towards the top of the subcloud layer the buoyancy flux decreases and can even become negative, indicating that, on average, rising plumes are negatively buoyant. If the plumes become saturated with water vapor, the latent heat release due to condensation enables them to rise further as positively buoyant clouds. The negative buoyancy fluxes just above the top of the cloud layer are due to entrainment of warm free tropospheric air. Longwave radiative cooling in the cloud top regions leads to buoyancy production, and as the cooled cloud parcels become heavier than the surrounding air they start sinking, leading to a positive buoyancy flux.

The imposed solar radiative heating of the cloud layer during daytime has a distinct effect on the turbulence structure of the boundary layer. In particular, the signature of a decoupled boundary layer structure is clearly visible from the double peak structure in $\overline{w'w'}$ and the rather low values for the TKE. As was observed at the end of the ASTEX Lagrangian (De Roode and Duynkerke 1996), the vertical profiles for the buoyancy flux and the vertical velocity variance during daytime and in the final stages of the Composite SCTs become similar to ones found in the dry convective boundary layer (Stevens 2007). Although this decoupled two-layer turbulence structure might be considered as a difficult condition to be represented by the LES models, there is a much better agreement in the turbulence profiles during daytime than during the night. For example, the differences in terms of $\overline{w'w'}$ profiles and TKE is much larger during nighttime. At first sight this seems at odds with the nighttime buoyancy fluxes which appear to agree pretty well. If we however zoom in at models that have slightly positive buoyancy fluxes at the top of the subcloud layer, for example MPI/UCLA and DHARMA, we find that they have the largest $\overline{w'w'}$ and TKE values. Stated more precisely, at 36 hrs from local noon their $\overline{w'w'}$ profiles have a single peak in contrast to the other models that tend towards a double peak structure.

Bretherton and Wyant (1997) argued that the buoyancy flux at the top of the subcloud layer $\overline{w'\theta'_{\mathrm{v}}}_{,h}$ is key to the development of a decoupled boundary layer. Because the sign of $\overline{w'\theta'_{\mathrm{v}}}$ determines whether turbulence will be diminished or amplified, Figs. 10a-d present the time evolution of the flux ratio $r_{\theta_{\mathrm{v}}}$, which defines the flux at the top of the subcloud layer h

normalized by its surface value,

$$r_{\theta_\mathrm{v}} = \frac{\overline{w'\theta'_{\mathrm{v},h}}}{\overline{w'\theta'_{\mathrm{v,sfc}}}}. \tag{2}$$

Table 5 shows the mean values of r_{θ_v} for the daytime and nighttime periods. In particular during nighttime periods with positive r_{θ_v} values the boundary layer is found to be vertically well-mixed, whereas a negative r_{θ_v} is indicative for decoupling as characterized by a double peak structure in the vertical velocity variance profile. For the Composite cases all models quickly obtain a small or negative r_{θ_v} for the Fast case, whereas for the Slow case two models return to a positive r_{θ_v} during the second nighttime period 'N2'. However, similar to the daytime periods, at the end of the simulations the boundary layer becomes permanently decoupled, as indicated by r_{θ_v} which remains negative during the third nighttime period 'N3', except for EULAG.

Likewise the flux ratio r_{q_t} is defined similar to r_{θ_v}, and measures the fraction of the surface evaporation which is transported out of the subcloud layer. Figs. 10e-h and the conditionally sampled results in Table 5 show that r_{q_t} exhibits a clear diurnal cycle. During daytime $r_{q_\mathrm{t}} < 1$, which indicates that moisture accumulates in the subcloud layer, whereas during the first nighttime period the rate at which cumulus clouds transport water out of the subcloud layer exceeds the surface evaporation leaving a drying of the subcloud layer. In general r_{q_t} is larger during nighttime as compared during daytime.

4. Stratocumulus LWP budget

To understand what controls the LWP evolution and what leads to the LWP differences among the LES models we have assessed the effect of turbulence, radiation and drizzle on the LWP evolution, following its budget analysis by Van der Dussen et al. (2014),

$$\frac{\partial LWP}{\partial t} = \mathrm{Ent} + \mathrm{Base} + \mathrm{Rad} + \mathrm{Prec} + \mathrm{Subs}. \tag{3}$$

As noted by Ghonima et al. (2015) this budget equation is analogous to the cloud layer depth budget by Wood (2007) and is derived from the conservation equations for heat, water and mass, and the terms are defined by

$$
\begin{aligned}
\mathrm{Ent} &= \rho w_\mathrm{e}(\eta\Delta q_\mathrm{t} - \Pi\gamma\eta\Delta\theta_\mathrm{l} - h_\mathrm{cld}\Gamma_{q_\mathrm{l}}) \\
\mathrm{Base} &= \rho\eta\left[\overline{w'q_\mathrm{t}'}(z_\mathrm{b}) - \Pi\gamma\overline{w'\theta_\mathrm{l}'}(z_\mathrm{b})\right] \\
\mathrm{Rad} &= \frac{\eta\gamma}{c_\mathrm{p}}\left[F_\mathrm{rad}(z_\mathrm{t}) - F_\mathrm{rad}(z_\mathrm{b})\right] \\
\mathrm{Prec} &= -\rho[P(z_\mathrm{t}) - P(z_\mathrm{b})] \\
\mathrm{Subs} &= -\rho h_\mathrm{cld}\Gamma_{q_\mathrm{l}}\overline{w}(z_\mathrm{t}),
\end{aligned}
\tag{4}
$$

with ρ the density of air, η and γ are factors that include the Clausius-Clapeyron relation, c_p is the specific heat for dry air, $\Gamma_{q_\mathrm{l}} < 0$ is the lapse rate of the liquid water specific humidity, Π is the Exner function, P the drizzle rate, and the stratocumulus cloud layer depth $h_\mathrm{cld} = z_\mathrm{t} - z_\mathrm{b}$, where the heights of the mean stratocumulus cloud base z_b and cloud top z_t were diagnosed from the heights between which the cloud fraction is larger than 0.4. The thermodynamic factors arise because if the cloud layer is moistened, the release of heat due to condensation of water causes the temperature to rise, which enhances the saturation specific humidity, such that not the full amount of the added moisture becomes liquid. A similar arguments holds if heat is added to the cloud layer, as its warming effect will act to evaporate some liquid water causing a compensating cooling effect.

The turbulent flux at the top of the cloud layer has been substituted by the flux-jump relation (Lilly 1968), which states that the flux of a quantity ψ at the top of the boundary layer is proportional to the entrainment velocity and the jump of the quantity across an infinitesimally thin inversion layer, e.g. for q_t,

$$
\overline{w'q_\mathrm{t}'}_{z_\mathrm{t}} = -w_\mathrm{e}\Delta\overline{q_\mathrm{t}}. \tag{5}
$$

Application of this relation gives a more accurate estimation of the flux of θ_l at the top of the cloud layer, as the diagnosed slab-averaged Reynolds-averaged flux typically underestimates the entrainment flux due to the fact that the inversion layer has a finite depth. The inversion jumps of θ_l and q_t are shown in Fig. 11. The LWP budget analysis for the ASTEX case has been reported by Van der Dussen et al. (2016) to investigate why a reduction of the large-scale subsidence causes the stratocumulus cloud deck to persist longer despite an increase in the entrainment velocity. This study also demonstrated that a very good correspondence can be obtained between the actual and the LWP tendency as diagnosed from the rhs of (4). Because our analysis is based on hourly-mean processed data of fluxes and mean quantities, the residual in the LWP budget is larger than in Van der Dussen et al. (2016). Nevertheless some robust features emerge from the dominant LWP budget terms shown in Fig. 12 and the corresponding Table 6, which shows the mean results and the standard deviations during a full daytime or nighttime period. We note that model results were not used if stratocumulus was not detected during some part of the selection period. Specifically, for the Fast case stratocumulus disappeared in MOLEM and DHARMA during periods 'D2' and 'D3', respectively, and did not recover, while DALES and MPI/UCLA temporarily had no stratocumulus during period 'D3'. For the Reference case MOLEM had no stratocumulus during 'D3'. For ASTEX no stratocumulus was present for DALES, SAM, MOLEM and DHARMA during period 'D2'.

The entrainment drying and warming effects are represented by $\mathrm{Ent}_{\mathrm{dry}}$ and $\mathrm{Ent}_{\mathrm{heat}}$ (the first two terms on the rhs of Ent), and likewise the Rad term has been split in a longwave and a shortwave contribution, $\mathrm{Rad}_{\mathrm{LW}}$ and $\mathrm{Rad}_{\mathrm{LW}}$, respectively. Longwave radiative cooling and cloud base moisture fluxes are the dominant terms which support the increase of the LWP. During daytime absorption of solar radiation tends to diminish the LWP. Its cloud layer warming effect acts to stabilize the cloud layer with respect to the subcloud layer, and as a result the input of moisture from below the cloud layer diminishes. Secondly, as the solar warming counteracts the destabilization due to longwave cooling at the cloud top, the cloud layer thinning due to entrainment of relatively warm and dry air also decreases. If the cloud layer becomes sufficiently thin or broken, we find that the longwave radiative cooling also strongly decreases. The EULAG model has the strongest longwave cooling effect, which apparently prohibits the stratocumulus cloud layer to break up for the Composite cases (see Fig. 3). Note that the state of the atmospheric column above the LES domain was prescribed for all cases, and the differences in the downward radiative fluxes at the top of the LES domain are therefore due to different radiative transfer schemes used in the LES models.

The budget analysis indicates that the imbalance of a couple of rather large contributions to the LWP tendency determines the actual LWP tendency. It also clarifies the role of entrainment. The Fast case has the smallest inversion jumps of θ_{l} as compared to the Reference and Slow cases. Because of this relatively weak thermal stability it has the largest entrainment rates, resulting in the largest cloud thinning effects due to the mixing of relatively warm and dry air from just above the inversion.

The cloud thinning effect due to precipitation is very small except for the ASTEX case during the first nighttime period. The difference in drizzle between the ASTEX and the Composite cases can be understood qualitatively from a drizzle parameterization at the cloud base height derived from observations by Comstock et al. (2004),

$$P_{\mathrm{cb}} = 0.37 \left(\frac{LWP}{N_{\mathrm{d}}} \right)^{1.75}, \tag{6}$$

which thus depends on the LWP and the cloud droplet concentration number N_{d} which is set to 100 cm^{-3} in the simulations. VanZanten et al. (2005) derived a similar relation. The three Composite cases have typical maximum LWP values of the order of 100 gm^{-2}, for which the parameterization above gives a drizzle rate of 11 Wm^{-2}. For higher LWP values such as found for the ASTEX case, the drizzle rate becomes more significant too, with values of 38 and 77 Wm^{-2} for LWP values of 200 and 300 gm^{-2}, respectively. The ASTEX case is the only simulation which starts during nighttime during which the stratocumulus cloud tends to thicken. It also has a rather cold and moist free troposphere, which tends to weaken its capability to thin the stratocumulus layer by entrainment.

Van der Dussen et al. (2013) showed from additional sensitivity experiments for the ASTEX case that the difference in the LWP is mainly attributable to differences in the precipitation rate. They also found that stronger precipitating stratocumulus had less entrainment of warm and dry inversion air at its top. During daytime model differences in LWP are also diminished by solar radiative heating of the cloud layer. This mechanism is particularly clear during the third daytime period 'D3' of the Fast and Reference case simulations by EULAG. The LWP in this model is much higher than in the others (see Figs. 3f and g), which causes a much stronger cloud thinning tendency due to the absorption of solar radiation (Figs. 12f and g).

5. Subcloud layer heat and moisture budgets

The behaviour of the surface SHF and LHF during the transitions is very different in the sense that the SHF becomes approximately constant at about 10 $\mathrm{Wm^{-2}}$, whereas the LHF tends to increase with time during the Lagrangian advection of the cloudy air mass (see Figs. 3q-x). A classical framework to explain the time evolution of surface fluxes is the mixed-layer model (MLM), which assumes a vertically well-mixed boundary layer (Lilly 1968; Schubert et al. 1979; Nicholls 1984). The values of the decoupling parameters α_{q_t} and α_{θ_l} indicate that this assumption is not appropriate for relatively deep boundary layers. On the other hand, since the subcloud layer is vertically well mixed, the MLM framework may be applied to this lower part of the boundary layer.

a. Evolution of the subcloud-layer height

Figs. 3a-d show that the gradual increase of the subcloud layer height, which approximately coincides with the cumulus cloud base height, reduces significantly during the final stages of the simulations. The time evolution of the subcloud mixed layer height h can be expressed in terms of the mass budget equation (Neggers et al. 2006),

$$\frac{\partial h}{\partial t} = E + \overline{w}|_h - M, \tag{7}$$

where E is a positive term that represents the entrainment process which mixes air into the subcloud layer from above, $\overline{w}|_h$ is the large-scale vertical velocity at the top of the subcloud layer which is negative for the cases considered here, and $M > 0$ is related to the shallow cumulus mass flux which acts as a sink term. Because the relative humidity (RH) in a vertically well mixed layer increases with height, an initial deepening of the subcloud layer depth h will subsequently lead to higher RH values at its top. This will trigger shallow cumulus clouds whose mass flux will reduce the height of the mixed layer, and hence the RH at its top. In this way the cumuli act as a kind of valve that will maintain an approximate constant RH at the top of the subcloud layer (Bretherton et al. 2004).

b. Analysis of the results

To study the behaviour of the surface heat fluxes we will apply a mixed layer model to the subcloud layer. This model assumes a quasi-steady state, which means that temporal changes in conserved thermodynamic variables are constant with height. This allows to obtain simple solutions for the vertical fluxes, which in this framework only depend on the values at the bottom and the top of the mixed layer, and the net effect of diabatic processes. In fact, if we approximate the mixed-layer height to be constant in time, and if we express the sea surface temperature as a linear function of time, it is possible to obtain analytical expressions for the thermodynamic evolution of the subcloud layer provided that we close the system with use of the flux ratios r_{θ_v} and r_{q_t}, respectively. Table 7 presents the notation for the initial conditions, the time-dependent surface boundary conditions, the definitions of the time scales of the system as derived in the Appendix, and the constants C_1, C_2 and C_3. In particular, we find that the mixed-layer values for θ_v and q_t change in time according to,

$$\theta_{\mathrm{v,ml}}(t) = \gamma_{\theta_\mathrm{v}} t + C_1 + C_2 \exp^{-t/\tau_{\theta_\mathrm{v}}}, \tag{8}$$

$$q_{\mathrm{t,ml}}(t) = \frac{q_{\mathrm{sat,sfc,0}}}{1 + \frac{\tau_q}{\tau_{\mathrm{CC}}}} \exp^{t/\tau_{\mathrm{CC}}} + C_3 \exp^{-t/\tau_q} + \Delta_h S_{q_\mathrm{t}} \tau_q, \tag{9}$$

where the operator Δ_h gives the difference of the diabatic flux across the subcloud layer.

Table 8 presents the time scales for the SCT cases, based on the average subcloud layer values from all the LES models. The tendency of the SST was obtained from a linear regression. For all SCT cases the mean value of r_{q_t} is slightly less then unity, which reflects the fact that the subcloud layer is moistening. For the three Composite cases the mean depth of the subcloud layer is slightly less than 800 m and the mean horizontal wind speed in the subcloud layer U_ml is almost identical. As a result the subcloud layer time scales τ_CC and τ_{θ_v} are also very similar.

For a sufficiently long simulation time, $t >> \tau_{\theta_\mathrm{v}}$, the memory term in the solution for $\theta_\mathrm{v,ml}$, i.e. the last term in Eq. (8) which includes information about the initial state, vanishes. Interestingly, it follows from Eqs. (A-5) and (A-11) that

$$\theta_\mathrm{v,sfc} - \theta_\mathrm{v,ml} = (\gamma_{\theta_\mathrm{v}} - \Delta_h S_{\theta_\mathrm{v}})\tau_{\theta_\mathrm{v}}. \tag{10}$$

The constant difference between the subcloud and surface values of θ_v has an important consequence for the surface buoyancy flux, which according to Eq. (A-3) becomes constant in time,

$$\overline{w'\theta'_\mathrm{v}}_\mathrm{,sfc} = \frac{(\gamma_{\theta_\mathrm{v}} - \Delta_h S_{\theta_\mathrm{v}})h}{1 - r_{\theta_\mathrm{v}}}. \tag{11}$$

The equilibrium surface buoyancy flux value is thus proportional to the depth of the subcloud layer and to the horizontal gradient of the sea surface along the path of the air mass. The values of the solution for the SCTs are also presented in Table 8. The analytic solutions give rather small values for $\overline{w'\theta'_\mathrm{v}}_\mathrm{,sfc}$, and well explain the behavior of the SHF (see Figs. 3q-t). The SHF can be expressed in terms of the surface fluxes of θ_v and q_t as,

$$\mathrm{SHF} \approx \rho c_\mathrm{p}(\overline{w'\theta'_\mathrm{v}}_\mathrm{,sfc} - \epsilon_I \overline{\theta} \overline{w'q'_\mathrm{t}}_\mathrm{,sfc}), \tag{12}$$

with θ the potential temperature just above the surface and c_p the specific heat of dry air. For $\overline{w'\theta'_\mathrm{v}}_\mathrm{,sfc} = 0.015$ mKs^{-1} the upper limit of the SHF is about 16 Wm^{-2}. The surface moisture flux tends to diminish the SHF. For example, if the LHF is 100 Wm^{-2} it will lower the SHF by about 7 Wm^{-2}.

With aid of Eqs. (A-3), (A-7), and (A-14) we can express a general solution for the surface humidity flux,

$$\overline{w'q'_\mathrm{t}}_\mathrm{,sfc} = C_\mathrm{d} U_\mathrm{ml} \left[\frac{q_\mathrm{sat,sfc,0} \exp^{t/\tau_\mathrm{CC}}}{\frac{\tau_\mathrm{CC}}{\tau_q} + 1} - C_3 \exp^{-t/\tau_q} \right], \tag{13}$$

which predicts that $\overline{w'q'_{\mathrm{t}}}_{,\mathrm{sfc}}$ will tend to increase exponentially with time. Substituting the mean values from the simulations displayed in Table 8 demonstrates that the analytical results for the final hour of the simulations give realistic estimates as compared to the LES results. To put the results into perspective, Fig. 13 shows analytical solutions for several values of $r_{q_{\mathrm{t}}}$. We have neglected the evaporation of drizzle, which for the three Composite cases is less than 1 Wm^{-2} across the subcloud layer. We used the surface forcing and initial conditions from the reference case, in addition to its mean subcloud-layer properties. Because the flux ratio $r_{q_{\mathrm{t}}}$ is a measure of the moisture flux divergence across the subcloud layer, it controls the evolution of the moisture in this layer. We notice that its value has a strong impact on the evolution of the LHF. Because the LHF is proportional to the difference between $q_{\mathrm{t,ml}}$ and $q_{\mathrm{sat,sfc,0}}$, a stronger removal of subcloud moisture will trigger a higher LHF. Furthermore, we note that $r_{q_{\mathrm{t}}} = 1$ represents a 'zero-flux divergence' of moisture in the subcloud layer, which implies that all the moisture that is evaporated from the surface is transported out of the subcloud layer by updrafts. This condition is equivalent to $q_{\mathrm{t,ml}}$ being constant in time, which follows directly from $\tau_q = \infty$ according to Eqs. (A-14) and (A-15).

In summary, the MLM analysis of the subcloud layer evolution during its Lagrangian advection well explains the LES results. For a decoupled boundary layer with a constant subcloud layer height, and a fixed value for $r_{\theta_{\mathrm{v}}}$, we find that $\overline{w'\theta'_{\mathrm{v}}}_{,\mathrm{sfc}}$ becomes constant in time while the surface saturation specific humidity dependency on the SST according to Clausius-Clapeyron forces $\overline{w'q'_{\mathrm{t}}}_{,\mathrm{sfc}}$ to grow exponentially in time. An interesting difference is found with the first Lagrangian MLM study on stratocumulus by Schubert et al. (1979). Their experiment 1 has a similar set up as our subcloud layer MLM analysis, with the SST varying linearly in time, and constant values for the wind speed and large-scale divergence. For a vertically well-mixed stratocumulus layer they found a gradual increase in the surface value of $\overline{w'\theta'_{\mathrm{v}}}$.

6. Conclusions

Four Lagrangian stratocumulus to shallow cumulus transition experiments were performed with six different LES models. The cases differ predominantly in terms of the amplitude and timescale of the transition. The LES models agree remarkably well in the representation of the evolution of the mean states. For all cases the structure of the boundary layer transforms from a vertically well mixed layer to one in which the subcloud and cloud layers appear as two separated mixed layers, with the stratocumulus layer being warmer and drier as compared to the subcloud layer, a situation which is referred to as decoupling (Nicholls 1984; Bretherton and Wyant 1997). The difference in the thermodynamic state of the subcloud and cloud layers increases for deeper boundary layers, which is found to be in a qualitative agreement with aircraft observations analysed by Wood and Bretherton (2004). The general good agreement between the models in the representation of the boundary-layer evolution can be partly explained by drizzle and solar heating of the cloud layer. Thicker cloud layers such as found for the ASTEX case will produce more precipitation and will absorb more solar radiation during daytime, and vice versa. In this way both processes act to diminish intermodel differences in the LWP. For the Composite cases the earliest timing of the break up of the stratocumulus layer is found for the Fast case, which is predominantly due to a slightly stronger entrainment warming and drying as compared to the Reference and Slow cases.

Superposed to this picture where the boundary layer is deepening due to increasing SSTs, there is a diurnal cycle associated with the absorption of solar radiation within the cloud layer. The models agree well in terms of LWP during the day, but less so in terms of LWP during night. The opposite is true for the cloud cover, which varies considerably considerably among the LES models during daytime. The EULAG model tends to maintain a closed cloud deck which can be attributed to its radiation scheme which gives a somewhat stronger longwave radiative cooling in the cloud layer. The SHF is small and of the order of

10 Wm^{-2}, whereas the LHF tends to increase with time for all cases.

The time evolution of the surface heat fluxes can be well explained by means of a simple mixed-layer model that is applied to the subcloud layer, and which uses generic bulk features found from the LES results as boundary conditions. Specifically the model makes use of the facts that the subcloud layer depth becomes almost constant in time, and that the buoyancy flux at the top of the subcloud layer tends to approach a fixed negative fraction of the surface value, similar to what is found for the dry convective boundary layer and cumulus-topped boundary layers. The critical quantity that controls the magnitude of the change in the surface evaporation is the moisture flux at the top of the subcloud layer. The fact that the specific humidity in the subcloud layer increases with time indicates that on average the surface moisture flux is larger than the value at the top of the subcloud layer. The LWP budget analysis shows that during periods with stronger turbulence, i.e. during nighttime, a stronger injection of subcloud layer moisture into the stratocumulus cloud base is accompanied by a stronger entrainment drying.

Fig. 14 presents a schematic of the main findings of the Lagrangian SCTs. The SHF remains rather small during the equatorwards advection of the air mass, while the LHF gradually increases. During nighttime the longwave radiative cooling acts to destabilize the cloud layer, which tends to generate more turbulence and a higher entrainment rate at the cloud top. Due to stronger turbulence in the cloud layer during the night, subcloud layer moisture is transported towards the stratocumulus at a rate that exceeds the surface evaporation during the first night of the three Composite cases, and also during the second night of the Slow case. This enhanced moisture flux feeds the stratocumulus with liquid water, thereby competing against the cloud thinning tendency by an increased entrainment of warm and dry air from just above the inversion. Overall we find that the nocturnal stratocumulus cloud deck is able to recover from a broken to a closed structure. During daytime the cloud layer is heated by absorption of solar radiation. This stabilises the cloud layer with respect to the subcloud layer, which hinders the vertical turbulent transport of subcloud layer moisture to the cloud layer. The warming by the sun, and the reduced moisture input at the base of the stratocumulus causes it to thin and to break up.

The representation of the moisture transport from the top of the subcloud mixed layer to the stratocumulus layer, and the entrainment of free tropospheric dry air at the top of the stratocumulus, are essential ingredients to capture the SCT. In fact, in a study on the representation of the SCT in large-scale models by Neggers (2015) it is found that SCMs favor a break-up of stratocumulus for inversion conditions that are different to each individual model. The presence of such modes may be indicative of a local hydrological cycle that is distinctively different among the models. The finding that the degree of decoupling has an important consequence for the LWP suggests that the decoupling parameters can be a helpful quantity in evaluating parameterization schemes for cloud-topped boundary layers (Dal Gesso et al. 2014). The 3D instantaneous LES (thermo-) dynamic fields may be further used to evaluate parameterizations used in global models.

SCT cases such as discussed here have been simulated to study the effect of changes in the large-scale forcing conditions in the Hadley cell under climate change conditions to assess its possible impact of the pace of the transition. For example, Bretherton and Blossey (2014) investigated and explained the effect of a perturbed radiative forcing, the overall tropical warming and changes in the inversion stability on the SCT. Likewise, Van der Dussen et al. (2016) used the LWP budget equation to investigate why a decrease in the large-scale subsidence extends the lifetime of stratocumulus despite an increase in the entrainment rate. In addition, both studies investigated the effect of applying a uniform insolation (constant in time) on the SCTs, which showed that the bulk evolution of the SCT in terms of boundary-layer deepening is rather similar. Kazil et al. (2015) investigated the effect of the wind speed on the SCT. They found that a higher wind speed leads to a larger entrainment rate and a faster growth of the boundary layer, caused by an enhanced buoyant production of turbulence kinetic energy (TKE) from latent heat release in cloud updrafts.

Acknowledgments.

The investigations were done as part of the European Union Cloud Intercomparison, Process Study & Evaluation Project (EUCLIPSE) project, funded under Framework Program 7 of the European Union. The set up of the Composite transition cases and the LES simulations with MPI/UCLA were supported by the Alexander von Humboldt foundation and the Max Planck Institute for Meteorology. The simulations with the Dutch LES model were sponsored by the National Computing Facilities Foundation (NCF) for the use of supercomputer facilities. DHARMA simulations used resources of the National Energy Research Scientific Computing Center, which is supported by the Office of Science of the U.S. Department of Energy under contract DE-AC02-05CH11231, and the NASA High-End Computing (HEC) Program through the NASA Advanced Supercomputing (NAS) Division at Ames Research Center. The simulations with SAM were supported by NOAA MAPP grant NA13OAR4310104. EULAG simulations used resources of the National Center for Atmospheric Research, which is sponsored by the National Science Foundation. We thank Erwin de Beus for his kind technical assistance, Chris Bretherton and three reviewers for their suggestions which helped to improve the manuscript.

Appendix A. A mixed-layer model for the subcloud layer

The budget equation for an arbitrary conserved thermodynamic variable ψ in a horizontally homogeneous atmosphere reads,

$$\frac{d\overline{\psi}}{dt} = -\frac{\partial \overline{w'\psi'}}{\partial z} - \frac{\partial \overline{S_\psi}}{\partial z} \tag{A-1}$$

where S_ψ is a diabatic source term. A vertical integration from the surface to the top of the subcloud layer h gives an expression for the vertical mean value ψ_{ml},

$$\frac{\partial \psi_{\mathrm{ml}}}{\partial t} = \frac{\overline{w'\psi'}_{\mathrm{sfc}} - \overline{w'\psi'}_{h}}{h} + \frac{\overline{S_\psi}_{,\mathrm{sfc}} - \overline{S_\psi}_{,\mathrm{h}}}{h} \tag{A-2}$$

with the subscripts 'sfc' and 'h' denoting the surface and the top of the subcloud layer, respectively. Because we will apply the budget equation to an air mass that is being advected by the horizontal mean wind, the mean horizontal advection terms can be neglected. The vertical advection term due to large-scale subsidence disappears because the assumption of well mixedness implies that the vertical gradient of ψ is zero.

In the following we use the notation as presented in Table 7. The surface flux is computed from a bulk formula,

$$\overline{w'\psi'}_{\mathrm{sfc}} = C_{\mathrm{d}} U_{\mathrm{ml}} (\psi_{\mathrm{sfc}} - \psi_{\mathrm{ml}}), \tag{A-3}$$

with $C_{\mathrm{d}} = 0.0012$ a bulk drag coefficient and U_{ml} the absolute value of the mean horizontal wind speed in the subcloud layer. To obtain analytical solutions we will assume that the sea surface temperature increases linearly with time,

$$\mathrm{SST}(t) = \mathrm{SST}_0 + \gamma_{\mathrm{T}} t. \tag{A-4}$$

Likewise we can express the surface virtual potential temperature as

$$\theta_{\mathrm{v,sfc}}(t) = \theta_{\mathrm{v,sfc,0}} + \gamma_{\theta_{\mathrm{v}}} t. \tag{A-5}$$

Since the change in $\theta_{\mathrm{v,sfc}}$ is dominated by changes in the SST we will approximate $\gamma_{\theta_{\mathrm{v}}} \approx \gamma_T (1 + \epsilon_I q_{\mathrm{sat,sfc,0}})/\Pi$, with Π the Exner function, and $\epsilon_I \approx 0.608$.

To compute the temporal variation of the surface moisture flux we will use an approximated form of the Clausius-Clapeyron equation (Stevens 2006),

$$q_{\mathrm{sat,sfc}}(\mathrm{SST}) = q_{\mathrm{sat,sfc,0}} \exp\left[\frac{L_{\mathrm{v}}}{R_{\mathrm{v}} \mathrm{SST}_0^2} (\mathrm{SST} - \mathrm{SST}_0)\right]. \tag{A-6}$$

For a linear increase of the temperature with time according to Eq. (A-4), $q_{\mathrm{sat,sfc}}$ will increase exponentially with time,

$$q_{\mathrm{sat,sfc}}(t) = q_{\mathrm{sat,sfc,0}} e^{t/\tau_{\mathrm{CC}}}. \tag{A-7}$$

Given this framework, the tendency for the virtual potential temperature in the subcloud layer $\theta_{\mathrm{v,ml}}$ is governed by the turbulent flux divergence which can be expressed in terms of the flux ratio $r_{\theta_{\mathrm{v}}}$,

$$\frac{\partial \theta_{\mathrm{v,ml}}}{\partial t} = (1 - r_{\theta_{\mathrm{v}}}) \frac{\overline{w'\theta'_{\mathrm{v,sfc}}}}{h} + \Delta_h S_{\theta_{\mathrm{v}}}, \tag{A-8}$$

with the source term representing the divergence of the net radiative flux. For the Composite SCTs the net longwave radiative flux varies between 1 and 2 Wm^{-2} during nighttime and daytime, respectively, across a vertical layer of 100 m below the clouds. The maximum solar radiative flux divergence is about 3 Wm^{-2} per 100 m, which leaves a negligibly small diurnal mean radiative forcing of the subcloud layer.

On the basis of the results presented in Fig. 3, we will ignore variations of h in time. In addition, we take $\Delta_h S_{\theta_\mathrm{v}}$ constant with time. Using Eqs. (A-3) and (A-5), this allows to express Eq. (A-8) as,

$$\frac{\partial \theta_{\mathrm{v,ml}}}{\partial t} = \frac{\theta_{\mathrm{v,sfc,0}} + \gamma_{\theta_\mathrm{v}} t - \theta_{\mathrm{v,ml}}}{\tau_{\theta_\mathrm{v}}} + \Delta_h S_{\theta_\mathrm{v}}. \tag{A-9}$$

The solution of Eq. (A-9) is given by

$$\theta_{\mathrm{v,ml}}(t) = \gamma_{\theta_\mathrm{v}} t + C_1 + C_2 \exp^{-t/\tau_{\theta_\mathrm{v}}}, \tag{A-10}$$

with

$$C_1 = \theta_{\mathrm{v,sfc,0}} - \gamma_{\theta_\mathrm{v}} \tau_{\theta_\mathrm{v}} + \Delta_h S_{\theta_\mathrm{v}} \tau_{\theta_\mathrm{v}}. \tag{A-11}$$

The constant C_2 follows from the initial condition,

$$C_2 = \theta_{\mathrm{v,ml,0}} - C_1 = \theta_{\mathrm{v,ml,0}} - \theta_{\mathrm{v,sfc,0}} + \gamma_{\theta_\mathrm{v}} \tau_{\theta_\mathrm{v}} - \Delta_h S_{\theta_\mathrm{v}} \tau_{\theta_\mathrm{v}}. \tag{A-12}$$

The budget equation for $q_{\mathrm{t,ml}}$ can be written as

$$\frac{\partial q_{\mathrm{t,ml}}}{\partial t} = -\frac{q_{\mathrm{t,ml}}}{\tau_q} + \frac{q_{\mathrm{sat,sfc,0}}}{\tau_q} e^{t/\tau_{\mathrm{CC}}} + \Delta_h S_{q_\mathrm{t}}. \tag{A-13}$$

The term $\Delta_h S_{q_\mathrm{t}}$ represents the amount of rain water that evaporates in the subcloud layer which we take constant in time. To allow for an analytical solution we will neglect diurnal variations in r_{q_t}, which gives a solution of the following form,

$$q_{\mathrm{t,ml}}(t) = \frac{q_{\mathrm{sat,sfc,0}}}{1 + \frac{\tau_q}{\tau_{\mathrm{CC}}}} \exp^{t/\tau_{\mathrm{CC}}} + C_3 \exp^{-t/\tau_q} + \Delta_h S_{q_\mathrm{t}} \tau_q, \tag{A-14}$$

with

$$C_3 = q_{\mathrm{t,ml,0}} - \frac{q_{\mathrm{sat,sfc,0}}}{1 + \frac{\tau_q}{\tau_{\mathrm{CC}}}} - \Delta_h S_{q_\mathrm{t}} \tau_q. \tag{A-15}$$

REFERENCES

Ackerman, A. S., and Coauthors, 2009: Large-eddy simulations of a drizzling, stratocumulus-topped marine boundary layer. *Mon. Weather Rev.*, **137**, 1083–1110.

Albrecht, B. A., C. S. Bretherton, D. W. Johnson, W. H. Schubert, and A. S. Frisch, 1995: The Atlantic stratocumulus transition experiment - ASTEX. *Bull. Amer. Meteorol. Soc.*, **76**, 889–904.

Blossey, P. N., and Coauthors, 2013: Marine low cloud sensitivity to an idealized climate change: The CGILS LES intercomparison. *J. Adv. Model. Earth Syst.*, **5**, 1–25.

Bony, S., and J.-L. Dufresne, 2005: Marine boundary layer clouds at the heart of tropical cloud feedback uncertainties in climate models. *Geophys. Res. Lett.*, **32**, doi:doi:10.1029/2005GL023851.

Bretherton, C. S., 2015: Insights into low-latitude cloud feedbacks from high-resolution models. *Phil. Trans. R. Soc. A.*, **373**, doi:http://dx.doi.org/10.1098/rsta.2014.0415.

Bretherton, C. S., P. Austin, and S. T. Siems, 1995: Cloudiness and marine boundary layer dynamics in the ASTEX Lagrangian experiments. Part II: Cloudiness, drizzle, surface fluxes and entrainment. *J. Atmos. Sci.*, **52**, 2724–2735.

Bretherton, C. S., and P. N. Blossey, 2014: Low cloud reduction in a greenhouse-warmed climate: Results from Lagrangian LES of a subropical marine cloudiness transition. *J. Adv. Model. Earth Syst.*, **6**.

Bretherton, C. S., S. K. Krueger, M. C. Wyant, P. Bechtold, E. V. Meijgaard, B. Stevens, and J. Teixeira, 1999: A GCSS boundary-layer cloud model intercomparison study of the first ASTEX Lagrangian experiment. *Boundary-Layer Meteorol.*, **93**, 341–380.

Bretherton, C. S., J. R. McCaa, and H. Grenier, 2004: A new parameterization for shallow cumulus convection and its application to marine subtropical cloud-topped boundary layers. Part I: Description and 1D results. *Mon. Weather Rev.*, **132**, 864–882.

Bretherton, C. S., and M. C. Wyant, 1997: Moisture transport, lower-tropospheric stability, and decoupling of cloud-topped boundary layers. *J. Atmos. Sci.*, **54**, 148–167.

Chung, D., G. Matheou, and J. Teixeira, 2012: Steady-state large-eddy simulations to study the stratocumulus to shallow cumulus cloud transition. *J. Atmos. Sci.*, **69**, 3264–3276.

Comstock, K. K., R. Wood, S. E. Yuter, and C. S. Bretherton, 2004: Reflectivity and rain rate in and below drizzling stratocumulus. *Quart. J. Roy. Meteorol. Soc.*, **130**, 2891–2918.

Dal Gesso, S., A. P. Siebesma, and S. R. de Roode, 2014: Evaluation of low-cloud climate feedback through single-column model equilibrium states. *Quart. J. Roy. Meteorol. Soc.*, doi:10.1002/qj.2398.

Dal Gesso, S., J. J. van der Dussen, A. P. Siebesma, S. R. de Roode, I. A. Boutle, Y. Kamae, R. Roehrig, and J. Vial, 2015: A single-column model intercomparison on the stratocumulus representation in present-day and future climate. *J. Adv. Model. Earth Syst.*, **0**, 0–0.

de Lozar, A., and J. P. Mellado, 2015: Mixing driven by radiative and evaporative cooling at the stratocumulus top. *J. Atmos. Sci.*, **72**, 4681–4700.

De Roode, S. R., and P. G. Duynkerke, 1996: Dynamics of cumulus rising into stratocumulus as observed during the first "Lagrangian" experiment of ASTEX. *Quart. J. Roy. Meteorol. Soc.*, **122**, 1597–1623.

De Roode, S. R., and P. G. Duynkerke, 1997: Observed Lagrangian transition of stratocumulus into cumulus during ASTEX: Mean state and turbulence structure. *J. Atmos. Sci.*, **54**, 2157–2173.

De Roode, S. R., and Q. Wang, 2007: Do stratocumulus cloud detrain? fire i data revisited. *Boundary-Layer Meteorol.*, **122**, 479–491.

Duynkerke, P. G., and Coauthors, 1999: Intercomparison of three- and one-dimensional model simulations and aircraft observations of stratocumulus. *Boundary-Layer Meteorol.*, **92**, 453–487.

Duynkerke, P. G., and Coauthors, 2004: Observations and numerical simulations of the diurnal cycle of the EUROCS stratocumulus case. *Quart. J. Roy. Meteorol. Soc.*, **130**, 3269–3296.

Gerber, H., G. Frick, S. P. Malinowski, S. L. Brenguier, and F. Burnet, 2005: Holes and entrainment in stratocumulus. *J. Atmos. Sci.*, **62**, 443–459.

Ghonima, M. S., J. R. Norris, T. Heus, and J. Kleissl, 2015: Reconciling and validating the cloud thickness and liquid water path tendencies proposed by R. Wood and J. J. van der Dussen et al. *J. Atmos. Sci.*, **72**, 20332040.

Heus, T., and Coauthors, 2010: Formulation of the Dutch Atmospheric Large-Eddy Simulation (DALES) and overview of its applications. *Geosci. Model Development*, **3**, 415–444, doi:10.5194/gmd-3-415-2010.

Kazil, J., G. Feingold, and T. Yamaguchi, 2015: Wind speed response of marine non-precipitating stratocumulus clouds over a diurnal cycle in cloud-system resolving simulations. *Atmos. Chem. Phys. Disc.*, **15**, 28 395–28 452, doi:doi:10.5194/acpd-15-28395-2015.

Khairoutdinov, M. K., and D. A. Randall, 2005: Cloud-resolving modeling of the ARM summer 1997 IOP: Model formulation, results, uncertainties and sensitivities. *J. Atmos. Sci.*, **60**, 607–625.

Klein, S. A., and D. L. Hartmann, 1993: The seasonal cycle of low stratiform clouds. *J. Climate*, 1587–1606.

Krueger, S. K., G. T. McLean, and Q. Fu, 1995: Numerical simulation of the stratus-to-cumulus transition in the subtropical marine boundary layer. Part I: Boundary-layer structure. *J. Atmos. Sci.*, **52**, 2839–2850.

Lilly, D., 1968: Models of cloud-topped mixed layers under a strong inversion. *Quart. J. Roy. Meteorol. Soc.*, **94**, 292–309.

Lock, A. P., 2009: Factors influencing cloud area at the capping inversion for shallow cumulus clouds. *Quart. J. Roy. Meteorol. Soc.*, **135**, 941–952.

Miller, M. A., and B. A. Albrecht, 1995: Surface-based observations of mesoscale cumulus-stratocumulus interaction during ASTEX. *J. Atmos. Sci.*, **52**, 2809–2826.

Moeng, C.-H., and Coauthors, 1996: Simulation of a stratocumulus-topped planetary boundary layer: Intercomparison among different numerical codes. *Bull. Amer. Meteorol. Soc.*, **77**, 261–278.

Neggers, R. A. J., 2015: Attributing the behavior of low-level clouds in large-scale models to sub-grid scale parameterizations. *J. Adv. Model. Earth Syst.*, doi:doi:10.1002/2015MS000503.

Neggers, R. A. J., B. Stevens, and J. D. Neelin, 2006: A simple equilibrium model for shallow-cumulus topped mixed layers. *Theor. Comput. Fluid Dyn.*, **20**, 305–322.

Nicholls, S., 1984: The dynamics of stratocumulus: Aircraft observations and comparisons with a mixed layer model. *Quart. J. Roy. Meteorol. Soc.*, **110**, 783–820.

Park, S., C. B. Leovy, and M. A. Rozendaal, 2004: A new heuristic lagrangian marine boundary layer cloud model. *J. Atmos. Sci.*, **61**, 3002–3024.

Prusa, J. M., P. K. Smolarkiewicz, and A. A. Wyszogrodzki, 2008: Eulag, a computational model for multiscale flows. *Comput. Fluids*, **37**, 1193–1207.

Sandu, I., and B. Stevens, 2011: On the factors modulating the stratocumulus to cumulus transitions. *J. Atmos. Sci.*, **68**, 1865–1881.

Sandu, I., B. Stevens, and R. Pincus, 2010: On the transitions in marine boundary layer cloudiness. *Atmos. Chem. Phys.*, **10**, 2377–2391.

Schubert, W. H., J. S. Wakefield, E. J. Steiner, and S. K. Cox, 1979: Marine stratocumulus convection. Part II: Horizontally inhomogeneous solutions. *J. Atmos. Sci.*, **36**, 1308–1324.

Siebesma, A. P., and Coauthors, 2003: A large eddy simulation intercomparison study of shallow cumulus convection. *J. Atmos. Sci.*, **60**, 1201–1219.

Simmons, A., S. Uppala, D. Dee, and S. Kobayashi, 2007: Era-Interim: New ECMWF reanalysis products from 1989 onwards. *ECMWF Newsletter*, **110**, 25–35.

Stevens, B., 2000: Cloud transitions and decoupling in shear-free stratocumulus-topped boundary layers. *Geophys. Res. Lett.*, **27**, 2557–2560.

Stevens, B., 2006: Bulk boundary-layer concepts for simplified models of tropical dynamics. *Theor. Comput. Fluid. Dyn.*, doi:DOI10.1007/s00162-006-0032-z.

Stevens, B., 2007: On the growth of layers of nonprecipitating cumulus convection. *J. Atmos. Sci.*, **64**, 2916–2931.

Stevens, B., G. Vali, K. Comstock, R. Wood, M. C. van Zanten, P. H. Austin, C. S. Bretherton, and D. H. Lenschow, 2005a: Pockets of open cells (POCs) and drizzle in marine stratocumulus. *Bull. Amer. Meteorol. Soc.*, **86**, 51–57.

Stevens, B., and Coauthors, 2001: Simulations of trade wind cumuli under a strong inversion. *J. Atmos. Sci.*, **58**, 1870–1891.

Stevens, B., and Coauthors, 2005b: Evaluation of large-eddy simulations via observations of nocturnal marine stratocumulus. *Mon. Weather Rev.*, **133**, 1443–1462.

Tsushima, Y., and Coauthors, 2015: Robustness, uncertainties, and emergent constraints in the radiative responses of stratocumulus cloud regimes to future warming. *Climate Dynamics*, 1–15, doi:10.1007/s00382-015-2750-7.

Van der Dussen, J. J., S. R. de Roode, S. D. Gesso, and A. P. Siebesma, 2015: An les model study of the influence of the free tropospheric thermodynamic conditions on the stratocumulus response to a climate perturbation. *J. Adv. Model. Earth Syst.*, **0**, 0–0.

Van der Dussen, J. J., S. R. de Roode, and A. P. Siebesma, 2014: Factors controlling rapid stratocumulus cloud thinning. *J. Atmos. Sci.*, **71**, 655–664.

Van der Dussen, J. J., S. R. de Roode, and A. P. Siebesma, 2016: How large-scale subsidence affects stratocumulus transitions. *Atmos. Chem. Phys.*, **16**, 691–701.

Van der Dussen, J. J., and Coauthors, 2013: The GASS/EUCLIPSE model intercomparison of the stratocumulus transition as observed during ASTEX: LES results. *J. Adv. Model. Earth Syst.*, **5**, 483–499, doi:10.1002/jame.20033.

VanZanten, M. C., B. Stevens, G. Vali, and D. H. Lenschow, 2005: Observations of drizzle in nocturnal marine stratocumulus. *J. Atmos. Sci.*, **62**, 88–106.

VanZanten, M. C., and Coauthors, 2011: Controls on precipitation and cloudiness in simulations of trade-wind cumulus as observed during RICO. *J. Adv. Model. Earth Syst.*, **3**, doi:doi:10.3894/JAMES.2011.3.5.

Vogelmann, A. M., and Coauthors, 2015: RACORO continental boundary layer cloud investigations: 1. Case study development and ensemble large-scale forcings. *J. Geophys. Res.*, **120**, doi:10.1002/2014JD022713.

Wang, Q., and D. H. Lenschow, 1995: An observational study of the role of penetrating cumulus in a marine stratocumulus-topped boundary layer. *J. Atmos. Sci.*, **52**, 650–666.

Webb, M. J., F. H. Lambert, and J. M. Gregory, 2013: Origins of differences in climate sensitivity, forcing and feedback in climate models. *Clim. Dyn.*, **40**, 677–707, doi:10.1007/s00382-012-1336-x.

Wood, R., 2007: Cancellation of aerosol indirect effects in marine stratocumulus through cloud thinning. *J. Atmos. Sci.*, **64**, 2657–2669.

Wood, R., 2012: Stratocumulus clouds. *Mon. Weather Rev.*, **140**, 2373–2423.

Wood, R., and C. S. Bretherton, 2004: Boundary layer depth, entrainment, and decoupling in the cloud-capped subtropical and tropical marine boundary layer. *J. Climate*, **17**, 3576–3588.

Zhang, M., and Coauthors, 2013: CGILS: Results from the first phase of an international project to understand the physical mechanisms of low cloud feedbacks in single column models. *J. Adv. Model. Earth Syst.*, 826–842, doi:10.1002/2013MS000246.

List of Tables

		ASTEX	Fast	Reference	Slow
p_{sfc}	hPa	1029.0	1015.9	1016.8	1017.6
latitude	^{0}N	34	25	25	25
longitude	^{0}W	25	125	125	125
date		13 June	15 July	15 July	15 July
Div	10^{-6} s^{-1}	-	1.9	1.86	1.84
$\mathrm{z_{Div}}$	km	1.6	2	2	2

TABLE 1. Details of the simulations. Div represents the large-scale divergence of the horizontal mean wind velocities, which is constant in time and constant up to a height of $\mathrm{z_{Div}}$, except for the ASTEX case in which the divergence varies with time.

LES model	Institute	References	Participants
DALES	TU Delft, The Netherlands	Heus et al. (2010)	Van der Dussen
MPI/UCLA	MPI-Hamburg, Germany	Stevens et al. (2005b)	Sandu
SAM	U. Washington, USA	Khairoutdinov and Randall (2005)	Blossey
MOLEM	UKMO, UK	Lock (2009)	Lock
DHARMA	NASA GISS, USA	Vogelmann et al. (2015)	Ackerman
EULAG	U. Warsaw, Poland	Prusa et al. (2008)	Jarecka

Table 2. Participating models and contributors.

	D1	N1	D2	N2	D3	N3
ASTEX		0–6	7–21	22–30	31–40	
Composite Cases	0–9	10–19	20–33	34–43	44–57	58–67

TABLE 3. Summary of periods of daytime (D1, D2 and D3) and nighttime (N1, N2 and N3), respectively, and the corresponding begin and end times in hours from the start of the simulations.

		Time	ASTEX	Fast	Reference	Slow
		D1		560 ± 30	530 ± 30	580 ± 20
		N1	260 ± 20	710 ± 40	720 ± 20	670 ± 20
$z_{\mathrm{cu,base}}$	m	D2	360 ± 10	770 ± 30	790 ± 10	740 ± 20
		N2	500 ± 20	750 ± 40	820 ± 30	880 ± 30
		D3	526 ± 9	810 ± 50	870 ± 20	890 ± 30
		N3		800 ± 50	840 ± 30	890 ± 30
		D1		1038 ± 6	968 ± 7	902 ± 6
		N1	770 ± 20	1260 ± 20	1120 ± 10	1010 ± 20
z_{i}	m	D2	1060 ± 50	1520 ± 50	1310 ± 30	1170 ± 30
		N2	1480 ± 50	1700 ± 100	1480 ± 60	1320 ± 40
		D3	1770 ± 60	1900 ± 100	1650 ± 80	1470 ± 50
		N3		2100 ± 200	1800 ± 100	1600 ± 80
		D1		30 ± 10	30 ± 10	51 ± 7
		N1	210 ± 20	80 ± 30	90 ± 20	80 ± 10
LWP	$\mathrm{gm^{-2}}$	D2	130 ± 20	30 ± 20	40 ± 10	50 ± 10
		N2	80 ± 20	50 ± 30	50 ± 20	90 ± 30
		D3	30 ± 10	30 ± 20	30 ± 10	40 ± 20
		N3		30 ± 20	40 ± 30	40 ± 20
		D1		0.98 ± 0.03	0.982 ± 0.009	0.9989 ± 0.0005
		N1	1.0 ± 0.0	0.99 ± 0.02	0.998 ± 0.001	0.9991 ± 0.0004
cc	0-1	D2	0.9994 ± 0.0004	0.9 ± 0.2	0.95 ± 0.03	0.98 ± 0.01
		N2	0.996 ± 0.005	0.9 ± 0.1	0.98 ± 0.02	0.997 ± 0.002
		D3	0.8 ± 0.2	0.7 ± 0.2	0.89 ± 0.08	0.96 ± 0.02
		N3		0.8 ± 0.2	0.93 ± 0.06	0.97 ± 0.02
		D1		0.65 ± 0.06	0.49 ± 0.04	0.39 ± 0.04
		N1	1.1 ± 0.2	1.07 ± 0.08	0.80 ± 0.05	0.62 ± 0.05
w_{e}	$\mathrm{cm\ s^{-1}}$	D2	1.21 ± 0.08	0.62 ± 0.09	0.52 ± 0.05	0.49 ± 0.04
		N2	1.49 ± 0.04	1.0 ± 0.1	0.83 ± 0.05	0.74 ± 0.02
		D3	0.71 ± 0.08	0.6 ± 0.1	0.54 ± 0.07	0.47 ± 0.05
		N3		0.9 ± 0.1	0.9 ± 0.1	0.79 ± 0.08
		D1		11 ± 1	7.1 ± 0.9	11 ± 1
		N1	7 ± 1	9 ± 1	6.2 ± 0.7	10 ± 1
SHF	$\mathrm{Wm^{-2}}$	D2	14 ± 1	7 ± 1	6.6 ± 0.7	9 ± 1
		N2	5.6 ± 0.8	9 ± 2	7 ± 1	7 ± 1
		D3	2.1 ± 0.2	8 ± 2	8 ± 1	6.6 ± 0.9
		N3		8 ± 2	9 ± 2	8 ± 1
		D1		104 ± 7	80 ± 3	90 ± 4
		N1	60 ± 10	126 ± 7	105 ± 4	103 ± 5
LHF	$\mathrm{Wm^{-2}}$	D2	100 ± 10	138 ± 7	119 ± 6	110 ± 6
		N2	94 ± 7	151 ± 7	130 ± 6	121 ± 6
		D3	56 ± 6	167 ± 9	153 ± 8	133 ± 8
		N3		169 ± 8	159 ± 8	150 ± 10
		D1		-410 ± 30	-420 ± 40	-350 ± 30
		N1	0 ± 0	0 ± 0	0 ± 0	0 ± 0
$\mathrm{SW_{net,sfc}}$	$\mathrm{Wm^{-2}}$	D2	-230 ± 30	-440 ± 60	-410 ± 40	-380 ± 40
		N2	0 ± 0	0 ± 0	0 ± 0	0 ± 0
		D3	-510 ± 80	-470 ± 80	-450 ± 60	-420 ± 50
		N3	0 ± 0	0 ± 0	0 ± 0	0 ± 0
		D1		30 ± 6	28 ± 3	23 ± 2
		N1	11.0 ± 0.7	27 ± 5	22.5 ± 0.9	22 ± 2
$\mathrm{LW_{net,sfc}}$	$\mathrm{Wm^{-2}}$	D2	19 ± 2	40 ± 10	36 ± 4	31 ± 2
		N2	24 ± 2	40 ± 10	33 ± 4	27.0 ± 0.9
		D3	40 ± 10	50 ± 10	46 ± 7	39 ± 4
		N3		50 ± 10	41 ± 7	37 ± 4

TABLE 4. Mean values and their standard deviations during the daytime and nighttime periods according to Table 3. The standard deviation is rounded to one significant digit. However, for compact notation we express, for example, $(10 \pm 2) \cdot 10^1$ as 100 ± 20.

	Time	ASTEX	Fast	Reference	Slow
	D1		-0.19 ± 0.08	-0.2 ± 0.1	0.1 ± 0.2
	N1	-0.2 ± 0.4	-0.3 ± 0.1	0.0 ± 0.4	0.4 ± 0.3
	D2	-0.20 ± 0.07	-0.17 ± 0.05	-0.20 ± 0.07	-0.2 ± 0.1
r_{θ_v}	N2	-0.20 ± 0.09	-0.17 ± 0.07	-0.21 ± 0.05	-0.1 ± 0.2
	D3	-0.09 ± 0.09	-0.14 ± 0.07	-0.16 ± 0.04	-0.19 ± 0.06
	N3		-0.16 ± 0.08	-0.17 ± 0.07	-0.21 ± 0.06
	D1		0.87 ± 0.07	1.1 ± 0.1	0.93 ± 0.05
	N1	1.09 ± 0.09	1.04 ± 0.07	1.26 ± 0.08	1.09 ± 0.05
	D2	0.83 ± 0.07	0.67 ± 0.07	0.72 ± 0.05	0.84 ± 0.08
r_{q_t}	N2	0.92 ± 0.05	0.95 ± 0.03	0.97 ± 0.05	1.1 ± 0.1
	D3	0.7 ± 0.2	0.79 ± 0.05	0.70 ± 0.07	0.67 ± 0.05
	N3		0.83 ± 0.07	0.91 ± 0.02	0.92 ± 0.07

TABLE 5. Mean values of the flux ratios r_{θ_v} and r_{q_t} and their standard deviations during the daytime and nighttime periods according to Table 3.

$\partial\mathrm{LWP}/\partial t$	$(\mathrm{gm^{-2}s^{-1}})$	Time	ASTEX	Fast	Reference	Slow
		D1		54 ± 9	54 ± 9	57 ± 6
		N1	62 ± 1	60 ± 8	61 ± 5	59 ± 6
$\mathrm{Rad_{LW}}$	$\frac{\eta\gamma}{c_\mathrm{p}}[\mathrm{LW_{net}}(z_\mathrm{t}) - \mathrm{LW_{net}}(z_\mathrm{b})]$	D2	65 ± 1	50 ± 10	50 ± 10	53 ± 9
		N2	67 ± 4	59 ± 7	56 ± 8	60 ± 6
		D3	57 ± 7	60 ± 10	50 ± 10	50 ± 10
		N3		50 ± 10	50 ± 10	56 ± 9
		D1		-20 ± 4	-19 ± 3	-25 ± 3
		N1	0.0 ± 0.0	-0.0 ± 0.0	-0.0 ± 0.0	-0.0 ± 0.0
$\mathrm{Rad_{SW}}$	$\frac{\eta\gamma}{c_\mathrm{p}}[\mathrm{SW_{net}}(z_\mathrm{t}) - \mathrm{SW_{net}}(z_\mathrm{b})]$	D2	-34 ± 2	-16 ± 4	-17 ± 4	-20 ± 4
		N2	0.0 ± 0.0	-0.0 ± 0.0	-0.0 ± 0.0	-0.0 ± 0.0
		D3	-19 ± 1	-19 ± 6	-14 ± 4	-16 ± 4
		N3		-0.0 ± 0.0	-0.0 ± 0.0	-0.0 ± 0.0
		D1		-51 ± 6	-45 ± 5	-41 ± 5
		N1	-70 ± 10	-87 ± 8	-74 ± 5	-63 ± 5
$\mathrm{Ent_{heat}}$	$-\rho w_\mathrm{e}\Pi\gamma\eta\Delta\theta_\mathrm{l}$	D2	-70 ± 6	-52 ± 6	-46 ± 5	-48 ± 4
		N2	-93 ± 5	-89 ± 7	-74 ± 7	-72 ± 3
		D3	-43 ± 5	-58 ± 8	-48 ± 5	-44 ± 5
		N3		-80 ± 10	-80 ± 10	-80 ± 10
		D1		-44 ± 5	-44 ± 5	-38 ± 4
		N1	-28 ± 6	-76 ± 6	-72 ± 4	-60 ± 4
$\mathrm{Ent_{dry}}$	$\rho w_\mathrm{e}\eta\Delta q_\mathrm{t}$	D2	-48 ± 5	-45 ± 5	-45 ± 5	-47 ± 4
		N2	-83 ± 4	-80 ± 10	-70 ± 5	-71 ± 2
		D3	-44 ± 6	-53 ± 6	-45 ± 5	-44 ± 4
		N3		-77 ± 7	-70 ± 10	-74 ± 8
		D1		11 ± 2	7 ± 2	4 ± 3
		N1	10 ± 7	17 ± 4	8 ± 5	0 ± 4
$\mathrm{Base_{heat}}$	$-\rho\eta\Pi\gamma\overline{w'\theta_\mathrm{l}'}(z_\mathrm{b})$	D2	21 ± 4	10 ± 2	8 ± 2	8 ± 2
		N2	16 ± 2	22 ± 2	13 ± 2	9 ± 3
		D3	0 ± 1	15.0 ± 0.6	12 ± 3	7 ± 2
		N3		20 ± 2	20.2 ± 0.8	14 ± 1
		D1		45 ± 4	47 ± 6	43 ± 2
		N1	37 ± 4	71 ± 7	70 ± 4	61 ± 4
$\mathrm{Base_{moist}}$	$\rho\eta\overline{w'q_\mathrm{t}'}(z_\mathrm{b})$	D2	44 ± 3	43 ± 4	44 ± 6	48 ± 4
		N2	62 ± 3	70 ± 10	69 ± 5	73 ± 6
		D3	34 ± 2	53 ± 6	46 ± 4	44 ± 5
		N3		73 ± 4	70 ± 10	72 ± 8
		D1		-1 ± 1	-1 ± 1	-1 ± 1
		N1	-40 ± 30	-3 ± 2	-3 ± 2	-2 ± 1
Prec	$-\rho[P(z_\mathrm{t}) - P(z_\mathrm{b})]$	D2	-18 ± 6	-2 ± 2	-2 ± 1	-2 ± 1
		N2	-4 ± 2	-3 ± 3	-2 ± 2	-3 ± 2
		D3	-1.3 ± 0.4	-2 ± 1	-2 ± 2	-2 ± 2
		N3		-4 ± 4	-3 ± 2	-2 ± 2
		D1		9 ± 2	7 ± 2	7.1 ± 0.6
		N1	41 ± 7	23 ± 5	18 ± 2	15 ± 1
$\mathrm{Ent_{z_i}}$	$-\rho w_\mathrm{e}h_\mathrm{cld}\Gamma_{q_\mathrm{l}}$	D2	33 ± 4	10 ± 2	9 ± 2	9 ± 1
		N2	33 ± 4	18 ± 6	14 ± 3	17 ± 3
		D3	14 ± 2	11 ± 4	8 ± 2	8 ± 2
		N3		15 ± 5	14 ± 6	13 ± 4

TABLE 6. Mean values and their standard deviations for some key LWP budget terms according to Eq. (4) during the daytime and nighttime periods according to Table 3.

initial surface conditions	SST_0 $\theta_{\mathrm{v,sfc,0}}$ $q_{\mathrm{sat,sfc,0}}$
initial mixed layer conditions	$\theta_{\mathrm{v,ml,0}}$ $q_{\mathrm{t,ml,0}}$
surface boundary conditions	$\gamma_{\mathrm{T}} \equiv \partial \mathrm{SST}/\partial t$ $\gamma_{\theta_{\mathrm{v}}} \equiv \partial \theta_{\mathrm{v,sfc}}/\partial t$
time scales	$\tau_{\theta_{\mathrm{v}}} \equiv \dfrac{h}{(1-r_{\theta_{\mathrm{v}}})C_{\mathrm{d}}U_{\mathrm{ml}}}$ $\tau_q \equiv \dfrac{h}{(1-r_{q_{\mathrm{t}}})C_{\mathrm{d}}U_{\mathrm{ml}}}$ $\tau_{\mathrm{CC}} = \dfrac{R_{\mathrm{v}}\mathrm{SST}_0^2}{L_{\mathrm{v}}\gamma_T}$
constants	$C_1 = \theta_{\mathrm{v,sfc,0}} - \tau_{\theta_{\mathrm{v}}}(\gamma_{\theta_{\mathrm{v}}} - \Delta_h S_{\theta_{\mathrm{v}}})$ $C_2 = \theta_{\mathrm{v,ml,0}} - \theta_{\mathrm{v,sfc,0}} + \tau_{\theta_{\mathrm{v}}}(\gamma_{\theta_{\mathrm{v}}} - \Delta_h S_{\theta_{\mathrm{v}}})$ $C_3 = q_{\mathrm{t,ml,0}} - \dfrac{q_{\mathrm{sat,sfc,0}}}{1+\frac{\tau_q}{\tau_{\mathrm{CC}}}} - \Delta_h S_{q_{\mathrm{t}}}\tau_q$

TABLE 7. Summary of the boundary conditions used for the subcloud mixed layer model, its time scales, and the definitions of the constants C_1, C_2 and C_3.

		Fast	Reference	Slow
γ_{T}	K day^{-1}	1.7	1.9	1.7
$r_{q_{\mathrm{t}}}$		0.8	0.9	0.9
U_{ml}	ms^{-1}	5.7	5.3	5.1
h	m	756	781	789
$\tau_{\theta_{\mathrm{v}}}$	h	25.6	28.7	30.0
τ_q	h	152	296	318
τ_{CC}	h	227	202	218
$\overline{w'\theta'_{\mathrm{v}}}$, Eq. (11)	mKs^{-1}	0.012	0.014	0.013
LHF, Eq. (13)	Wm^{-2}	165	170	162

TABLE 8. Average values as obtained during the entire run and from all the LES models, except for the surface fluxes which represent the analytical results at the end of the simulations.

List of Figures

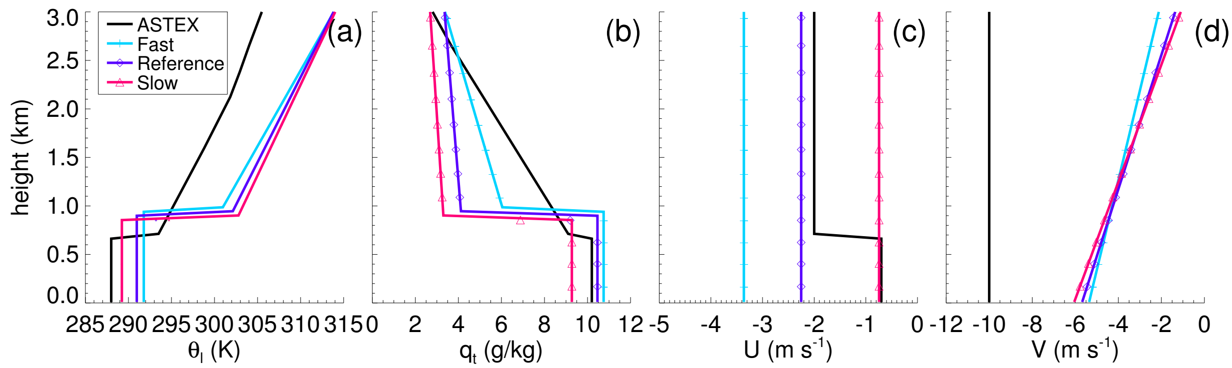

FIG. 1. Initial vertical profiles of (a) the liquid water potential temperature θ_l, (b) the total water specific humidity q_t, and the horizontal wind velocity components (c) U and (d) V for the ASTEX, Fast, Reference and Slow cases. The line styles are according to the legend.

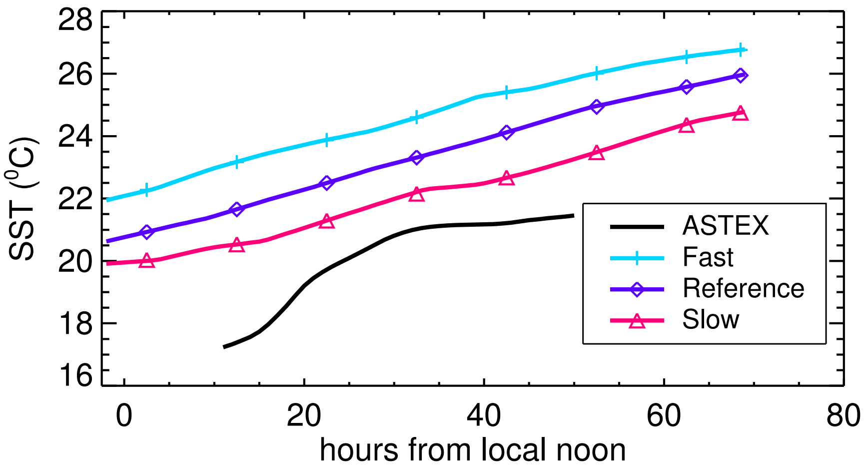

FIG. 2. Prescribed sea surface temperature for the ASTEX, Fast, Reference and Slow cases. The line styles are according to the legend.

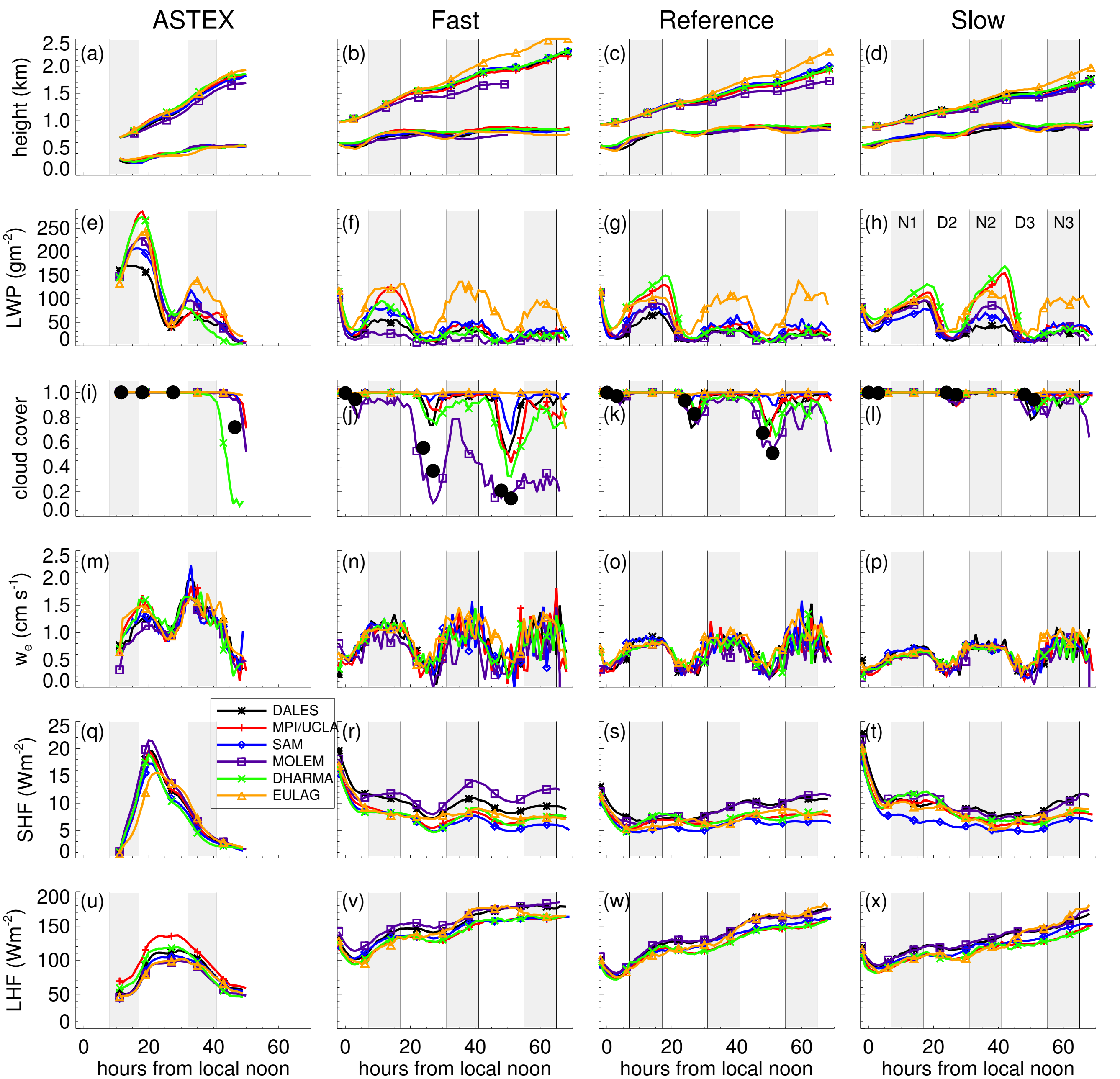

FIG. 3. Time series of the (a-d) lowest cumulus cloud base height (lower solid lines without symbols) and the mean inversion height (upper solid lines with symbols), (e-h) the domain-averaged liquid water path LWP, (i-l) the cloud cover, (m-p) the entrainment velocity w_{e}, (q-t) the sensible heat flux SHF and (u-x) the latent heat flux LHF. From left to right the columns present results of the ASTEX, Fast, Reference and Slow cases, respectively. The line styles are according to the legend displayed in figure q. The filled black big circles in i indicate the cloud cover as derived from aircraft observations, and in j,k,l they represent retrievals from the MODIS satellite along the trajectories of the Composite cases and can be considered as an upper bound of the real cloud fraction [see Appendix A of Sandu et al. (2010)].The grey shaded bands indicate periods of nighttime (denoted at the top of Fig. 3h) according to Table 3.

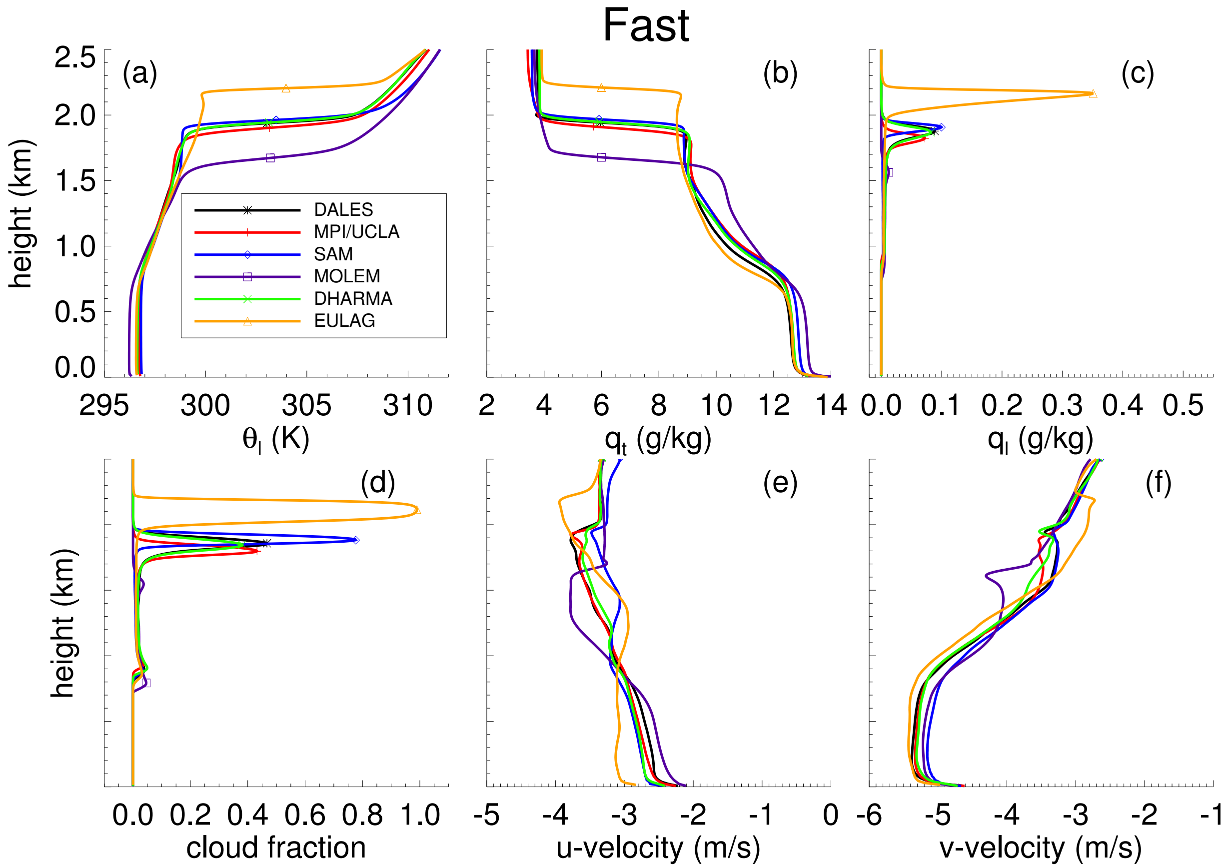

FIG. 4. Vertical profiles of (a) the liquid water potential temperature θ_l, (b) the total specific humidity q_t, (c) the liquid water specific humidity q_l, (d) the cloud fraction, (e) the east-west velocity U, and (f) the north-south velocity V for the Fast case. The lines represent hourly-mean horizontally slab averaged values obtained during the 48th hour from local noon. The line styles are according to the legend.

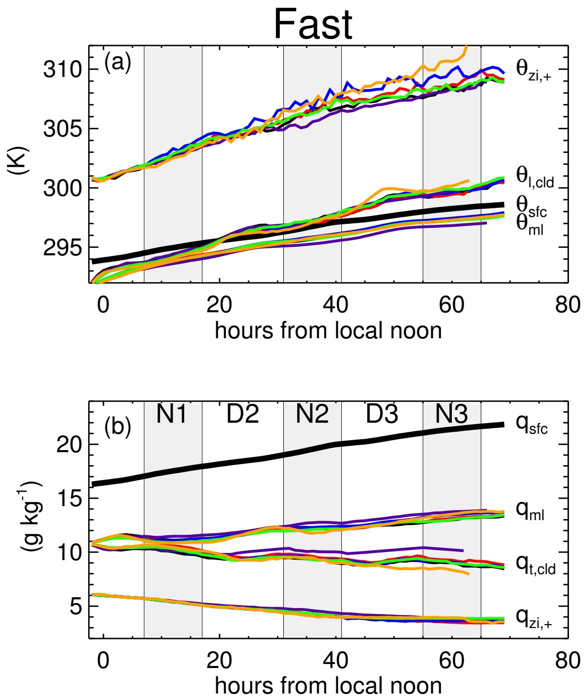

FIG. 5. Evolution of (a) the (liquid water) potential temperature and (b) the (total) specific humidity just above the inversion (z_i^+), and their vertical mean values in the subcloud (sub) and the stratocumulus cloud layer (cld) for the Fast case. For easy reference the prescribed values at the surface (sfc) are also plotted. The line styles are according to the legend as in Fig. 4a. The grey shaded bands indicate nighttime periods according to Table 3.

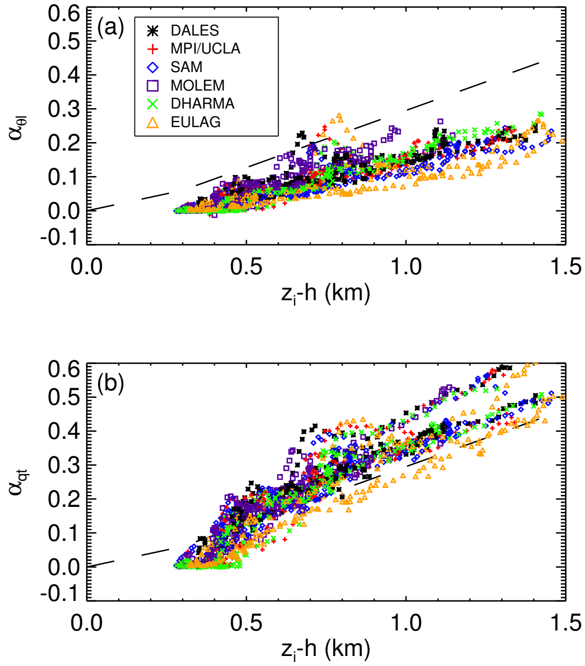

FIG. 6. The decoupling parameters (a) $\alpha_{\theta_\mathrm{l}}$ and (b) α_{q_t} as a function of the cloud layer depth. The dashed lines indicate a fit using the aircraft observations of α_{q_t} presented by Wood and Bretherton (2004), their Fig. 5. The symbols are according to the legend.

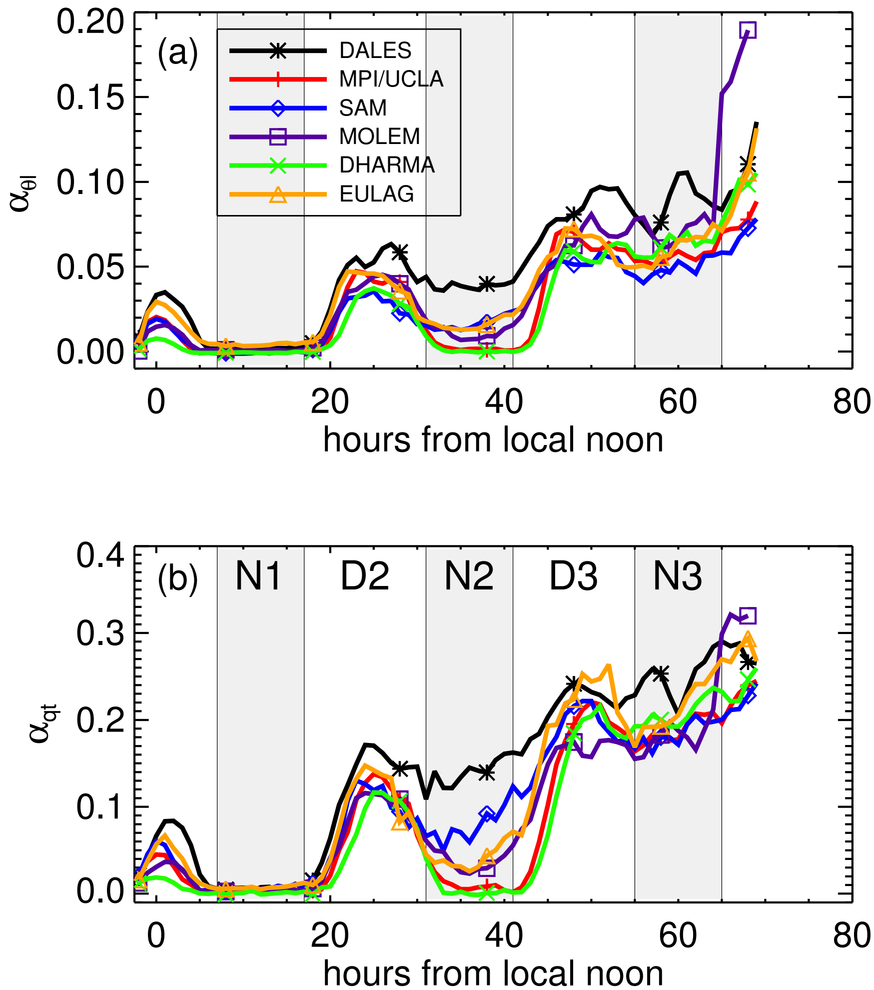

FIG. 7. The time evolution of the decoupling parameters of (a-d) α_{θ_l} and (e-h) α_{q_t} for the Slow case. The line colors and symbols are according to the legend. The grey shaded bands indicate nighttime periods according to Table 3.

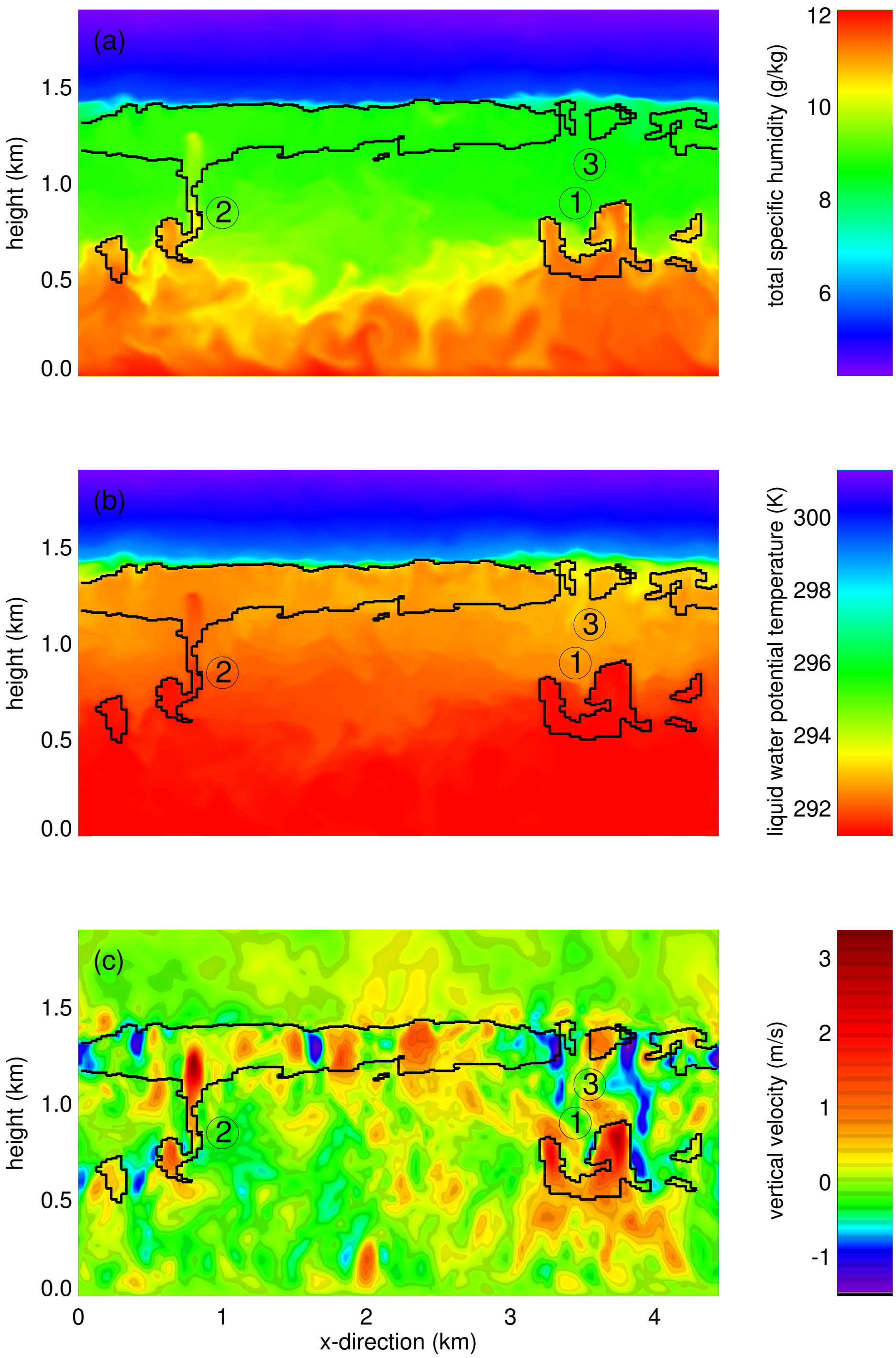

Fig. 8. Instantaneous fields in the vertical plane for (a) the total water specific humidity, (b) the liquid water potential temperature, and (c) the vertical velocity as obtained 36 hours from local noon from the DALES ASTEX run. The thick solid black lines indicate the contours of the cloud edges. See text for an explanation of the areas that are indicated by the encircled numbers.

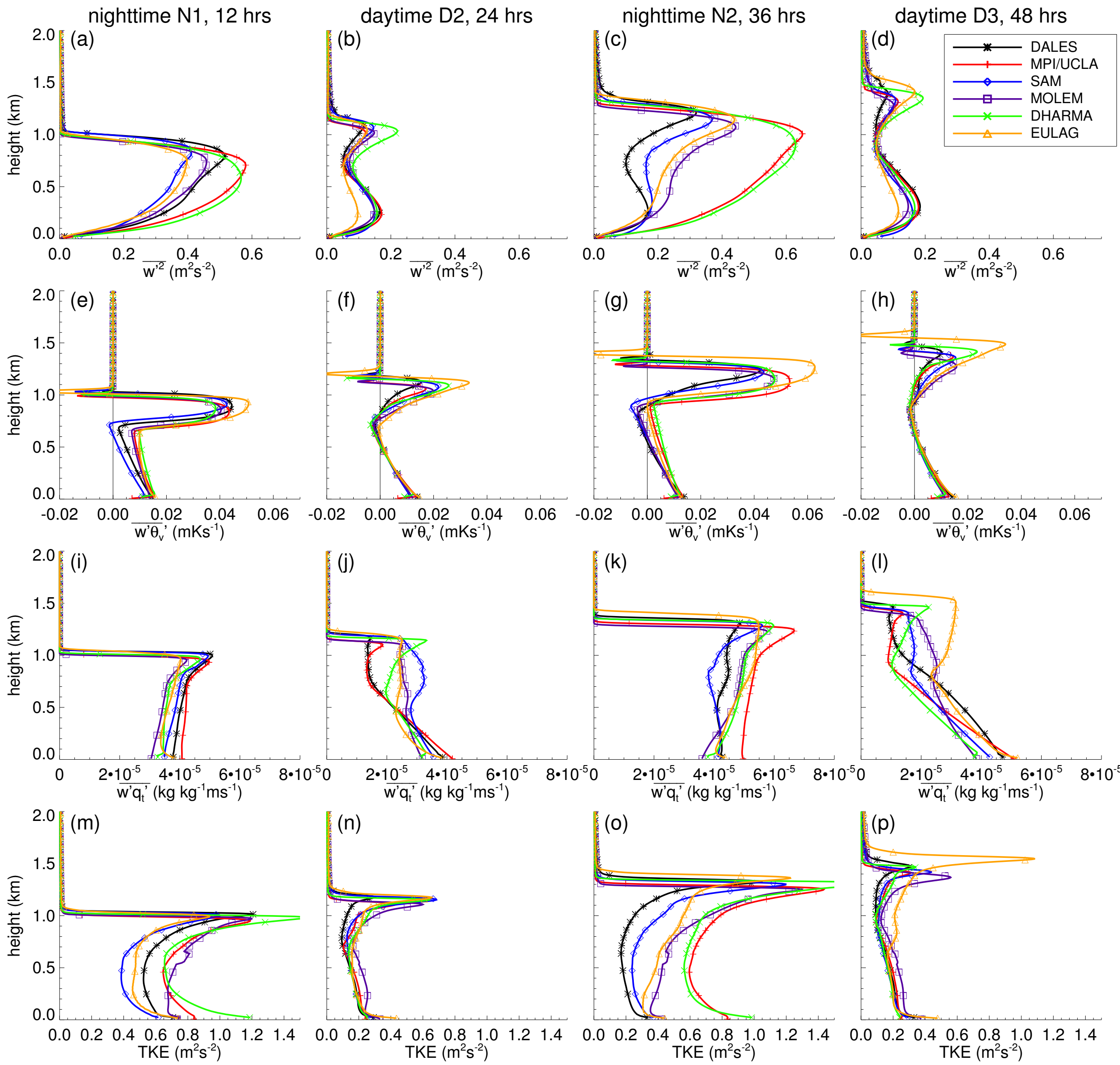

FIG. 9. Hourly-mean turbulence statistics for the 'Slow' case at four selected times. The profiles at 12 and 36 hrs from local noon are at midnight, and 24 and 48 hrs represent conditions during local noon. The first row (a-d) shows the vertical velocity variance, the second row (e-h) the virtual potential temperature flux, the third row (i-l) the total water specific humidity flux and the bottom row (m-p) the turbulent kinetic energy. The line colors and symbols are as in the legend shown in figure d. The thin black vertical line in the plots showing the virtual potential temperature flux indicates a zero value for easy reference.

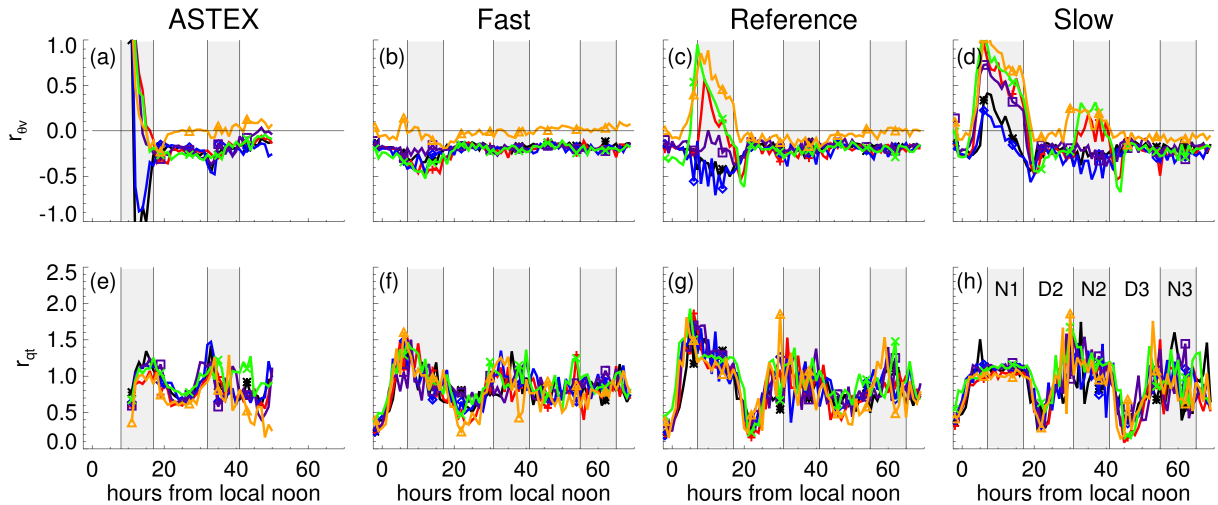

FIG. 10. The time evolution of the flux ratios for the (a-d) buoyancy (r_{θ_v}) and (e-h) the total water specific humidity (r_{q_t}) computed according to Eq. (2). The line styles are according to the legend. The grey shaded bands indicate nighttime periods according to Table 3. The line colors and symbols are as in the legend shown in Fig. 4a. The thin solid black line in a-d represents the zero line.

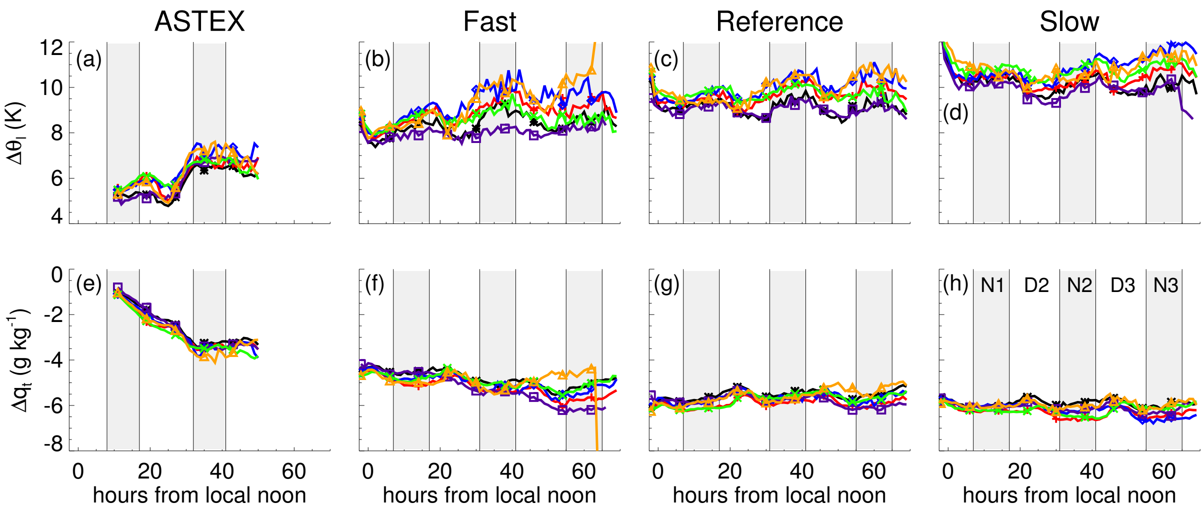

FIG. 11. Time evolution of the inversion jumps of (a-d) $\Delta\theta_l$ and (e-h) Δq_t. The line colors and symbols are as in the legend shown in Fig. 4a. The grey shaded bands indicate nighttime periods according to Table 3. The line colors and symbols are as in the legend shown in Fig. 4a.

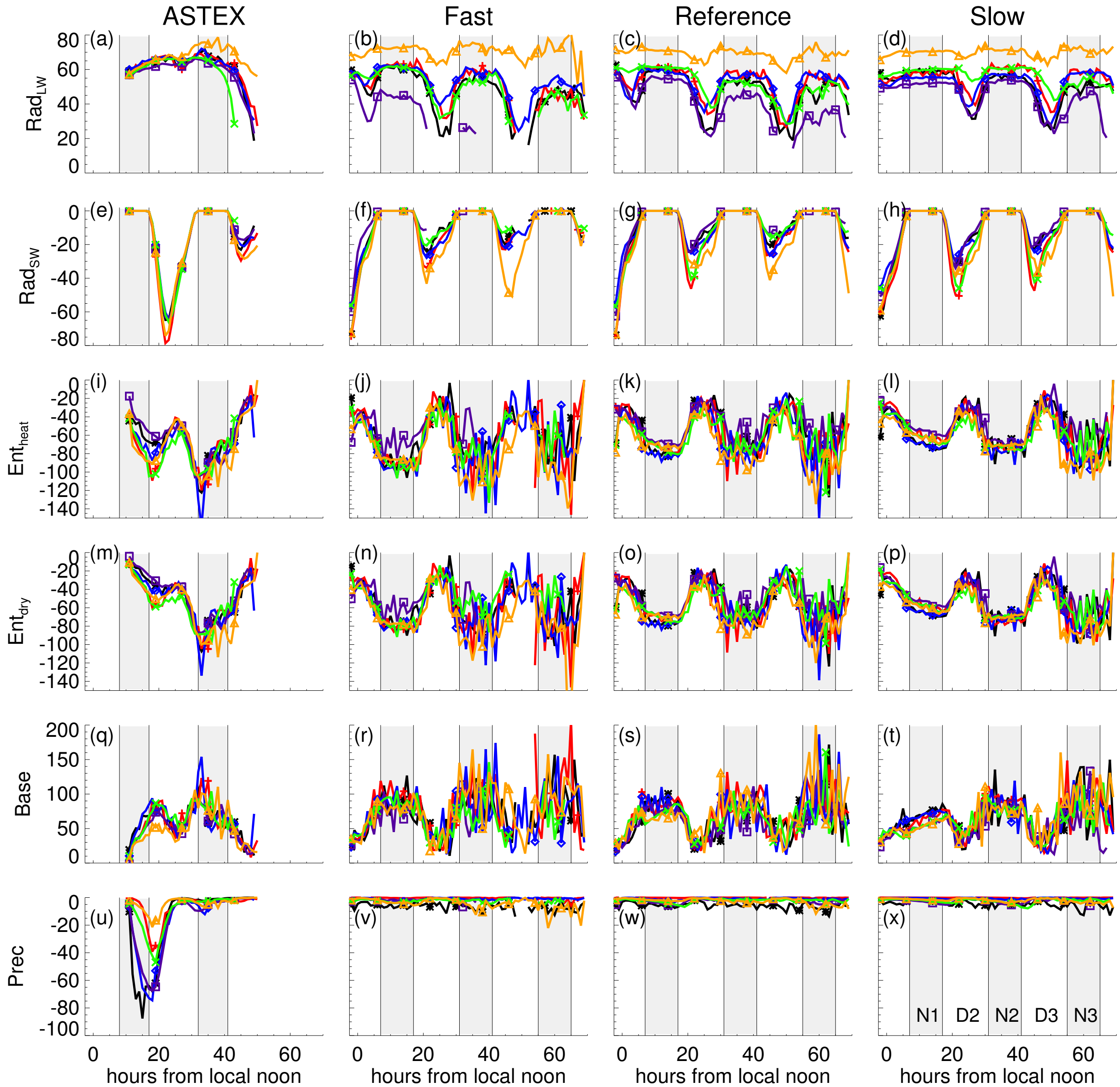

FIG. 12. Time evolution of the dominant terms in the LWP budget, with the variables displayed on the vertical axes denoting LWP tendencies in units of g m^{-2}h^{-1} due to (a-d) longwave radiative cooling (Rad$_{\mathrm{LW}}$) and (e-h) the absorption of solar radiation in the cloud layer (Rad$_{\mathrm{SW}}$), entrainment of (i-l) warm (Ent$_{\mathrm{heat}}$) and (m-p) dry inversion air (Ent$_{\mathrm{dry}}$), (q-t) cloud base fluxes of heat and moisture (Base), and (u-x) represent the LWP tendency due to drizzle (Prec). The grey shaded bands indicate nighttime periods according to Table 3. The line colors and symbols are as in the legend shown in Fig. 4a.

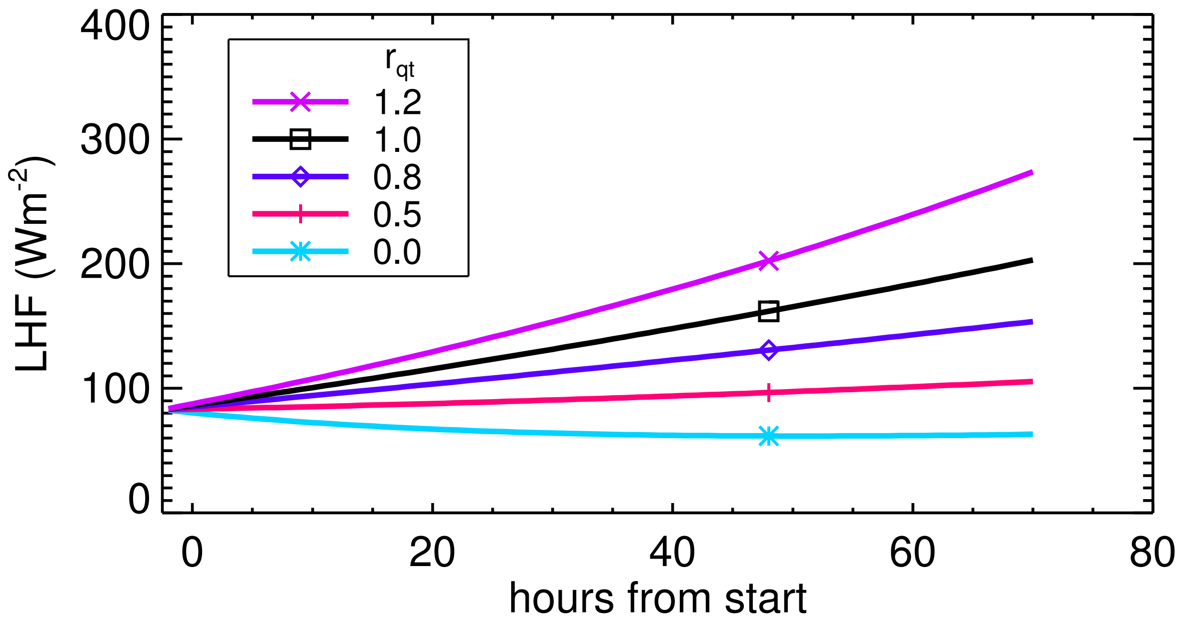

FIG. 13. The latent heat flux as a function of time and for different values of r_{q_t}, which measures the ratio of the total humidity flux at the top of the subcloud layer to its surface value. The line styles are according to the legend.

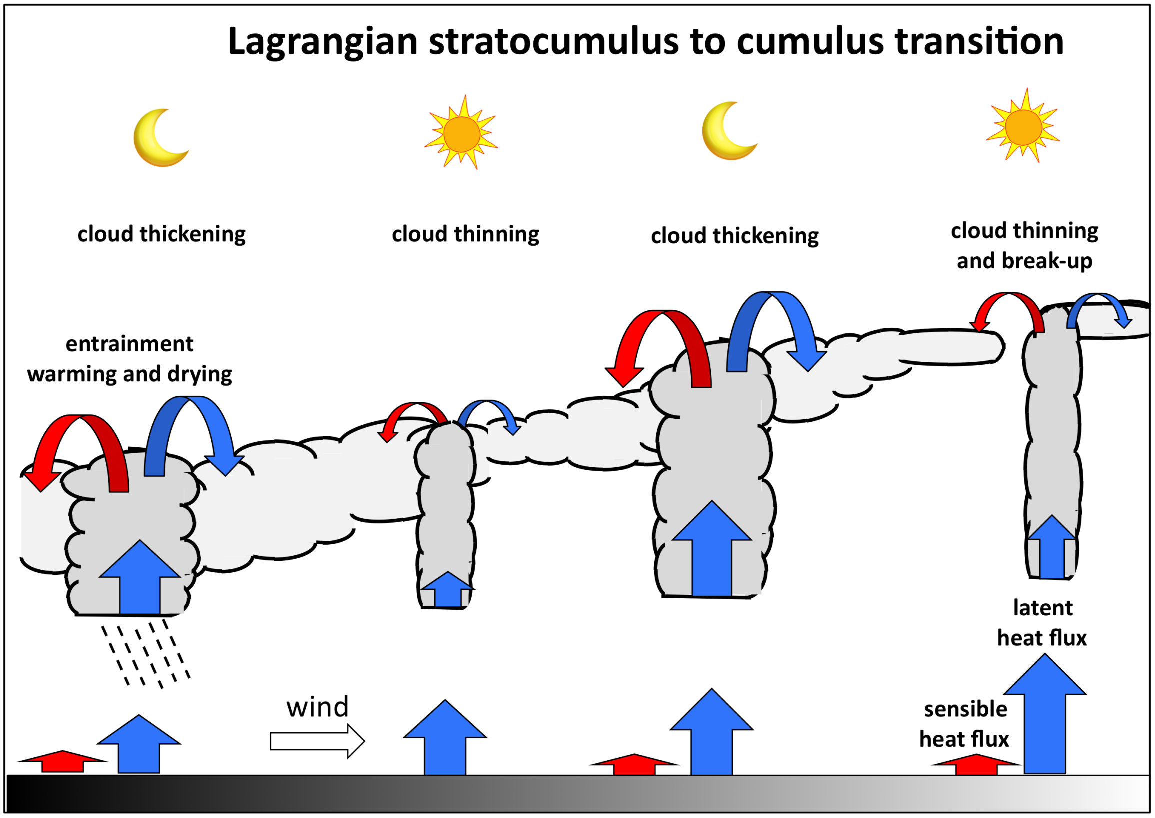

Fig. 14. Schematic showing the gradual break up of a stratocumulus cloud layer during its Lagrangian advection over an increasing SST. The vertical arrows represent the sensible and latent heat fluxes. During the night turbulence in the cloud layer intensifies, causing larger humidity fluxes at cloud base and cloud top.